Synthesis of oxide-based solid electrolyte for lithium batteries

By

Hirra Anwar

Reg. No. 00000318629

Session 2019-21

Supervised by

Dr. Ghulam Ali

A Thesis Submitted to the US-Pakistan Center for Advanced Studies in Energy in partial fulfillment of the requirements for the degree of

MASTER of SCIENCE in

Energy Systems Engineering

US-Pakistan Center for Advanced Studies in Energy (USPCAS-E)

National University of Sciences and Technology (NUST)

H-12, Islamabad 44000, Pakistan

June 2022

THESIS ACCEPTANCE CERTIFICATE

Certified that final copy of MS/MPhil thesis written by **Ms. Hirra Anwar** (Registration No. 00000318629), of US-Pakistan Center for Advanced Studies in Energy (USPCAS-E) has been vetted by undersigned, found complete in all respects as per NUST Statues/Regulations, is within the similarity indices limit and is accepted as partial fulfillment for the award of MS degree. It is further certified that necessary amendments as pointed out by GEC members of the scholar have also been incorporated in the said thesis.

Signature: ______________________________

Name of Supervisor: ________________________

Date: ________________________

Signature (HoD): ________________________

Date: ____________________________________

Signature (Dean/Principal): __________________

Date: ____________________________________

Certificate

This is to certify that work in this thesis has been carried out by **Ms. Hirra Anwar** and completed under my supervision in Synthesis and Energy Storage laboratory, US-Pakistan Center for Advanced Studies in Energy (USPCAS-E), National University of Sciences and Technology, H-12, Islamabad, Pakistan.

Supervisor:

Dr. Ghulam Ali
USPCAS-E
NUST, Islamabad

GEC member 1:

Dr. Zeeshan Ali
USPCAS-E
NUST, Islamabad

GEC member 2:

Dr. Mustafa Anwar
USPCAS-E
NUST, Islamabad

GEC member 3:

Dr. Sehar Shakir
USPCAS-E
NUST, Islamabad

HOD-ESE:

Dr. Rabia Liaquat
USPCAS-E
NUST, Islamabad

Dean/Principal:

Prof. Dr. Adeel Waqas
USPCAS-E
NUST, Islamabad

Dedication

To my parents, who supported me in every aspect of life and my siblings.

Acknowledgments

First and foremost, I am thankful to Almighty ALLAH who is the creator and author of knowledge. Indeed, without YOUR blessings, this mammoth task would not have been possible. And I acknowledge that without YOUR willingness and guidance, I would not have done a single task.

I am grateful to my parents for their unconditional love and sacrifices. I am forever in your debt for your encouragement, financial and moral support. Thank you for keeping confidence in me.

Dr. Ghulam Ali, I express my sincerest gratitude to you for this opportunity, for your teaching, mentorship, and patience throughout the research. It has been truly a privilege to work with you. I would like to thank my GEC members **Dr. Zeeshan Ali, Dr. Mustafa Anwar,** and **Dr. Sehar Shakir** for their guidance and help throughout my research.

I am also thankful to the staff of Synthesis and Energy Storage Lab specially **Engineer Naveed,** and Advanced energy materials lab engineer **Mr. Asghar Ali** who helped in my research and gave valuable advice during my experimentation. I am also grateful to the other lab staff, faculty members, and administration who were a part of this journey. I profusely thank my husband **Sheraz Khan Jadoon** for his immense support, always being there for me whenever I needed help. Also, all my friends for their support both academically and in general. And to life, an extraordinary experience with so many things to enjoy within a short span. Thank you for giving me so much in the years past, and for more to discover in the years to come.

Abstract

All-solid-state lithium batteries (ASSLBs) with high energy density, long cycle life, and wide voltage window have become a viable alternative to cope with safety issues of traditional lithium- ion batteries. The use of solid electrolyte eliminates numerous problems associated with liquid electrolytes, such as flammability, leaking and dendrites formation. Sodium super ionic conductors NASICON solid electrolytes are stable towards air and moisture and offer good mechanical and thermal stability. Among NASICON-type solid electrolytes lithium aluminum titanium phosphates (LATP) should have high ionic conductivity at room temperature, low interface impedance between electrode/electrolyte interface, and good compatibility with lithium metal to achieve high performance in ASSLBs.

In this work NASICON-type co-doped $Li_{1.3+x+y}Al_{0.3-x}Y_xTi_{1.7}Si_yP_{3-y}O_{12}$. (LAYTSP) (where x=0.01-0.1 and y=0.1-0.4) solid electrolyte is synthesized via conventional solid-state method at different sintering temperatures, and their intrinsic physical, chemical, and electrochemical properties are investigated using X-ray diffraction (XRD), scanning electron microscopy (SEM), Fourier transform infra-red spectroscopy (FTIR), and Xray photoelectron spectroscopy (XPS), electrochemical impedance spectroscopy (EIS). The LAYTSP powders have a homogeneous hexagonal shape and outstanding crystallinity, with the LAYTSP at 900 °C solid electrolyte having a high ionic conductivity of 1.81×10^{-5} S/cm. These findings show that this novel material is expected to be widely used in ASSLBs in the future.

Keywords: Lithium-ion batteries LIBs, Thermal Runaway TR, all solid-state electrolytes for lithium batteries ASSLBs, solid-state electrolyte SSE, NASICON solid electrolyte, oxide-based solid electrolyte.

Table of Contents

List of Figures

List of Tables

List of Publications

1. **Hirra Anwar**, Zeeshan Ali, Ghulam Ali “Investigation of electrochemical properties of Y and Si co-doped $Li_{1.3}Al_{0.3}Ti_{1.7}(PO_4)_3$ solid electrolyte for lithium batteries” **Journal of Alloys and compounds, 2022**

List of Abbreviations

LIBs	Lithium-ion batteries
TR	Thermal runaway
SSEs	Solid state electrolyte
EV	Electric vehicle
HEV	Hybrid electric vehicle
Li	Lithium
ASSLBs	All solid-state lithium-ion batteries
MOF	Metal organic framework
NASICON	Sodium superionic conductor
LISICON	Lithium superionic conductor
Li-ion	Lithium ion
Y	yttrium
RT	Room Temperature
Si	Silicon
XRD	X ray Diffraction
XPS	X ray photoelectron spectroscopy
SEM	Scanning Electron Microscopy
EIS	Electrochemical impedance spectroscopy
σ	Ionic conductivity
FTIR	Fourier transform infrared spectroscopy
EDS	Energy dispersive X-ray spectroscopy
V	Voltage

Chapter: 1 Introduction

1.1 Background

Energy exists in two main forms i.e., renewable (sun, wind, water, biomass etc.) and non-renewable (coal, oil, natural gas) energy resources. The non-renewable or conventional energy resources were used efficiently during 20th century in transport, industrial and power sectors. The use of renewable energy resources has gained great importance during the last 10 years due to the environmental hazards caused by the conventional sources and the depletion of the fossil fuels [1]. The renewable sources of energy are sustainable and environment friendly however, the non-reliability issue is a major limitation in replacing the conventional energy systems completely by renewable energy systems. Incorporating storage units with these energy systems can makes them reliable. Batteries have the potential when used as electrical storage in electric vehicles EVs to revolutionize the transport sector providing a substitute to petrol and diesel-powered cars [2]. Role of technology in renewable energy and electric storage toward a decarbonized energy future is quite evident. According to world issues monitor 2017 electrical storage comes under one of the high impact critical uncertainties [3]. Electrical storage technological improvements can play dynamic role to stamp out the main concerns affiliated with energy efficiency. Electric storage is still chiefly based on electrochemical secondary batteries. For storing energy, the evaluation of different storage mediums is done based on energy density. Energy per unit weight of electrochemical process dictates its applicability in portable devices [2]. Nickel hydride and Li ion batteries (LIBs) have made certain breakthroughs and have penetrated the mobile and transport markets such as laptops, tools, cameras, mobile phones, EVs, Hybrid electric vehicles (HEVs) [4] etc. [5]. Research groups are intensely focused on LIBs, in addition to other battery systems such as lithium air [6], lithium sulfur [7] and redox flow batteries [8].

LIBs are like conventional batteries in a way that in both redox reactions occurring at the interface between electrolyte and electrode while ions diffusion take place in the electrolyte however the notable difference is the solid-state mass diffusion [9].

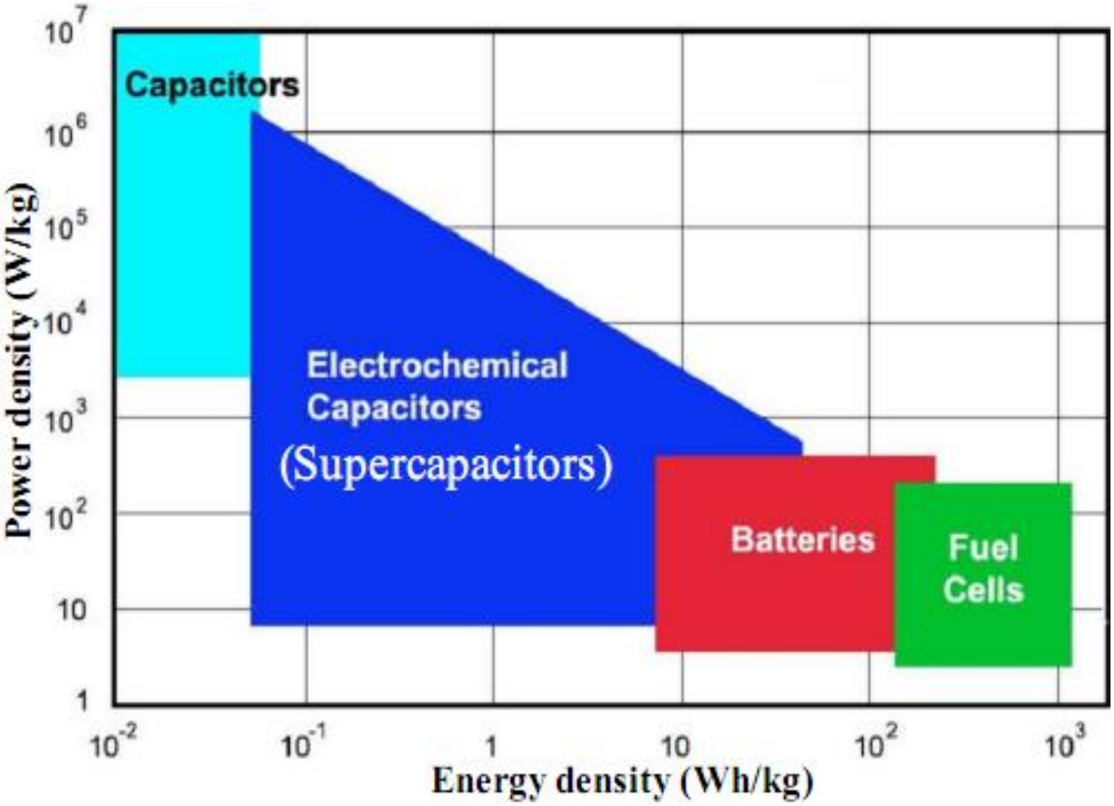

Figure 1.1: Electrochemical processes for electrical energy storage systems

1.1.1 Market Estimation for LIBs

Secure growth is estimated by Panasonic Group (Sanyo) for ESS market potential of the LIB. Simulation assuming continuation of purchase trend of battery keeping in view market survey and Li ion future price [10]. Community use for energy storage and investment substitution for distribution and transmission and the use of LIBs instead of lead acid battery considering its safe maintenance. Further assuming no lithium use concerning to energy storage. Keeping all these points in consideration indicates the progressiveness of LIBs especially in residential areas starting from 2017 [5].

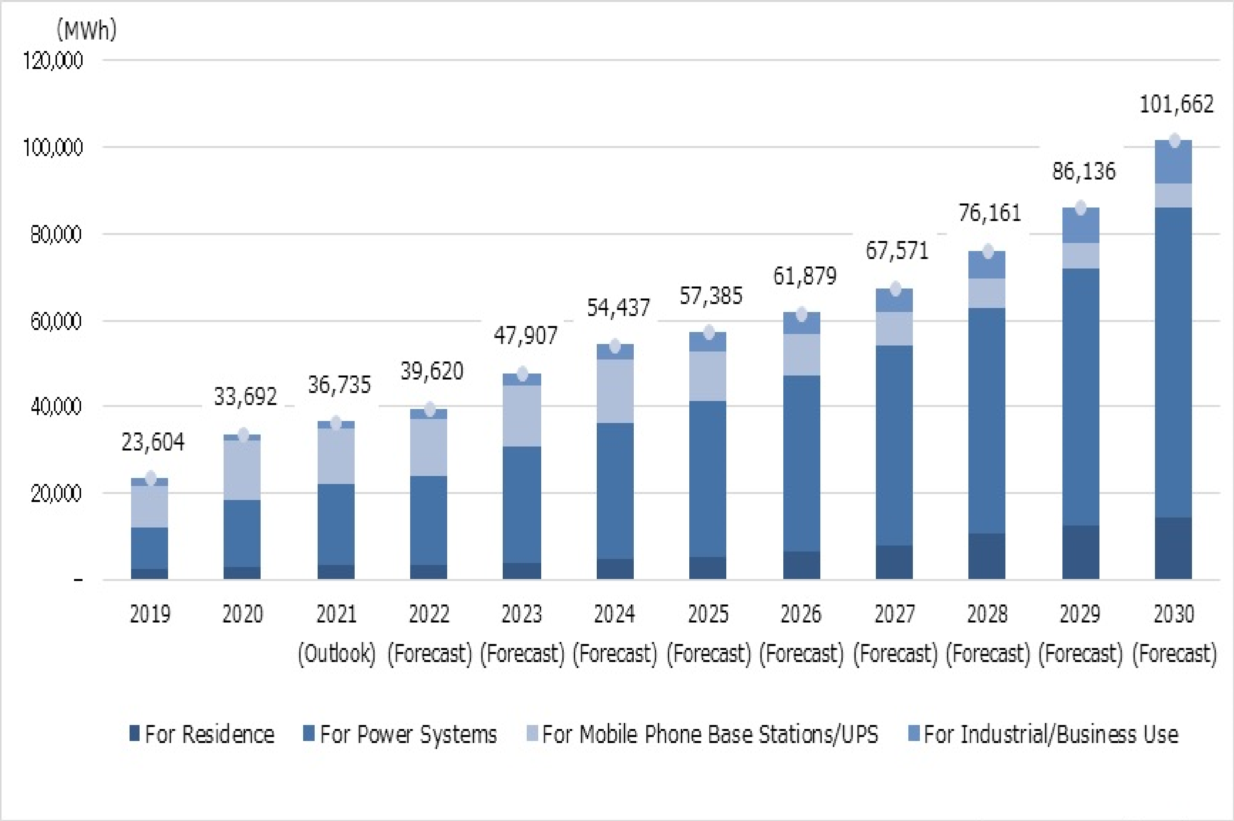

Figure 1.2: LIB global market published by Sanyo

1.2 Li ion Batteries

Lithium intercalation compounds are employed as positive and negative electrode materials in LIBs. The lithium ions intercalate and de-intercalate form the electrodes as the battery charges and discharges. “Rocking chair batteries” is also sometimes attributed to LIBs due to the rocking of lithium ion between positive and negative electrodes. more than 20 years ago Sony Co., Japan introduced lithium cobalt oxide ($LiCoO_2$) batteries as commercial LIBs [11]. This battery consisted of a layered type of compound namely $LiCoO_2$ as the cathode, the anode material was Graphite (C) while the electrolyte was gel polymer for the conduction of Li^+. Recently more research efforts have been devoted to electrode and electrolyte materials to achieve high energy density LIBs [12].

1.2.1 Early Development of Lithium-insertion Batteries

LIB’s journey begins with the Authority of UK Atomic energy publishing patent showing that in the material with the structural formula $A_xM_yO_2$ insertion and deintercalation of A_x is reversible,

M_y being a transition metal and A_x alkaline metal. HP-211 was then manufactured by SONY utilizing this patent in 1990 with a $LiCoO_2$/soft carbon system chemistry [13]. The mass production was started as a camcorder TR-1 application, the very next year however now with $LiCoO_2$/hard carbon [14].

1.2.2 Working of LIBs

During charging the electrons travel through the outer circuit form the cathode to the anode while the Li^+ ions are deintercalated from the host matrix of cathode and intercalated into the anode material. The reverse mechanism occurs on discharging i.e., the electrons through the outer circuit travels, powering various systems, from the anode towards the cathode where now electrochemical reduction occurs as lithium ions are intercalated into the host material [15].

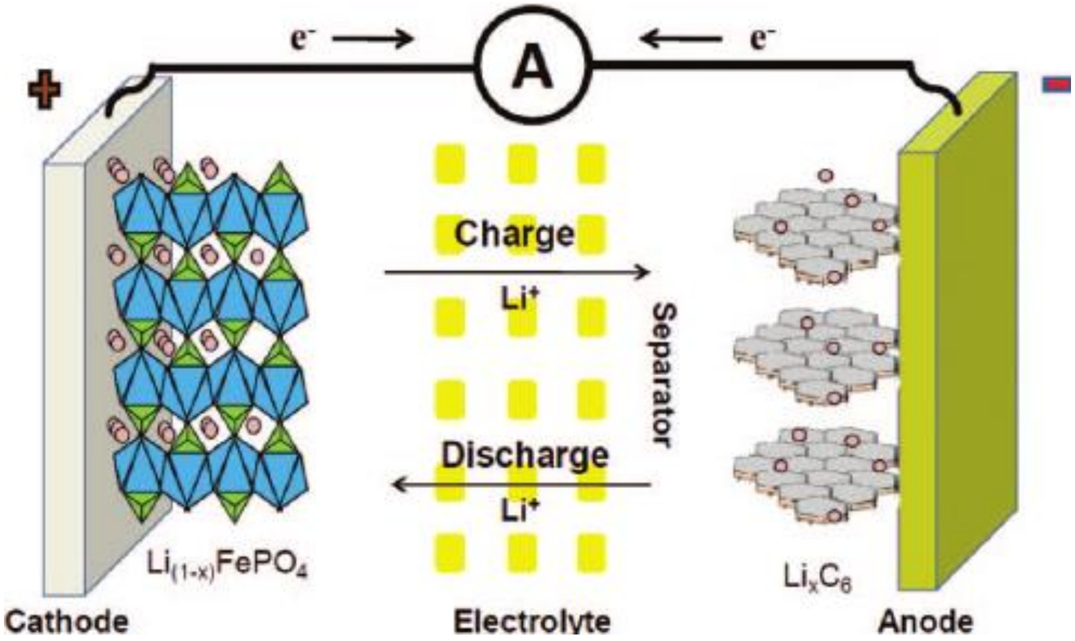

Figure 1.3: Schematic illustration of LIB working

1.2.3 Electrochemistry of LIBs

Electrochemistry of the battery can be described by cathode and anode undergoing an insertion reaction. Having layered or tunnel structures the anode and cathode material taking part in the insertion and extraction processes establishes an insertion mechanism comprising the movement of Li^+ cations. The source of lithium is cathode material as the lithium metal anodes have been replaced by graphitic carbon material. Half reaction of a redox reaction in case of lithium metal oxides of the form $LiMO_2$ (where M represents transition metal) and graphite as the anode is given by:

At the cathode side:

$$LiMO_2 \leftrightarrow Li_{1-x}MO_2 + xLi^+ + xe^-$$

At the anode side:

$$xLi^+ + xe^- + 6C \leftrightarrow Li_xC_6$$

During charging the transition metal oxide gets oxidized from M^{+3} to M^{+4}, whereas the opposite is true upon discharging as the transition metal is reduced from M^{+4} to M^{+3}.

1.2.4 Applications of LIBs

Dominating cell phone, computer, and camera power source, in addition to military/renewable and other numerous applications the LIB technology and industry is under vast expansion. In addition, the application of LIB in HEVs leaves question of safety regarding large scale batteries [9]. The use of expensive materials and components in the secondary lithium battery systems is a hindrance towards the growth rate of this industry.

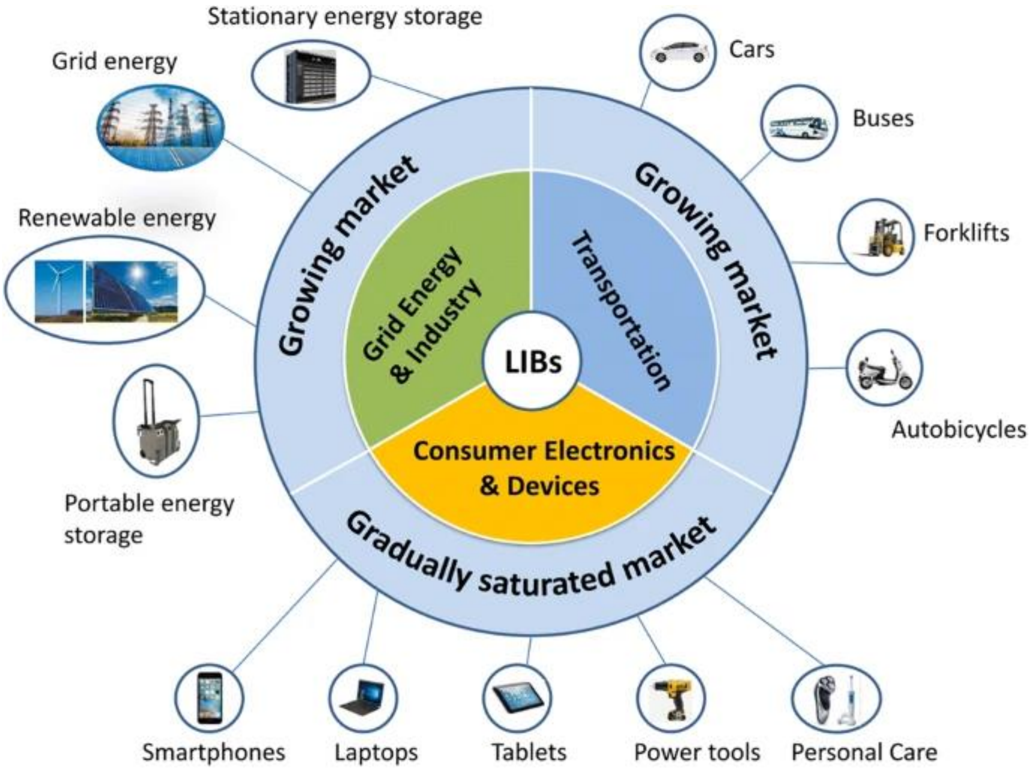

Figure 1.4: Application of LIBs

1.2.5 Safety issues associated with LIBs

The safety issues in LIBs are mostly caused by the failure of battery elements (cathode, anode, electrolyte, separators, and current collectors) and the failure of whole battery system caused during abuse conditions [17]. The battery system failure includes gas evolution, dendrites formation, thermal runway, overcharging, decomposition of current collectors etc [18].

1.2.5.1 Gas Evolution

In LIBs the electrolyte does not remain stable at high voltage level~4V and reacts with electrode materials at the electrode/electrolyte interface. These interface reactions occur continuously between the organic solvents in electrolyte and the cathode material and are the cause of gas evolution in LIBs [19]. The gas is generated in LIBs during these conditions:

1. Normal cycling
2. Overcharge
3. High temperature conditions
4. First charge process

During the first charge process a small amount of gas is evolved and the following gases are mainly evolved during first reaction carbon monoxide CO, hydrogen H_2 and ethylene C_2H_4. During normal cycling in the required voltage gas carbon dioxide CO_2, carbon monoxide, ethylene C_2H_4, methane CH_4, and ethane C_2H_6 are released. These gases are mostly generated during the oxidation and reduction of electrolyte at electrode surface. Carbon dioxide is generated by the oxidation reaction and the other gases are generated by the reduction reaction [20].

The overcharge conditions are associated with high rated oxidation and reduction reactions than normal cycling conditions. At cathode the O_2 gas is generated and at anode surface the H_2 gas is generated which contains small quantity of hydrocarbons. The gases released are the same as in normal operating conditions however, the amount of gas release is higher [21]. Similarly, the gases released during storage under high temperatures include carbon dioxide CO_2 at cathode surface and carbon monoxide CO at both electrode surfaces.

1.2.5.2 Dendrites Formation

One of the most important factors of internal short circuit in LIBs is the formation of dendrites on anode surface. The dendrites rupture the polymer separator and connect both electrodes causing an internal short circuit. It was observed that the higher current densities and incorporation of Li foil supports Li dendrite growth. The mechanism of short circuit involves the formation of dendrites when the potential starts decreasing after continuous voltage discharge for 38 hours and after 100 hours the single dendrites reach the positive electrode and causes internal short circuit.

1.2.5.3 Thermal runaway

The increase in temperature occurring from heat generation caused by the abuse conditions is known as thermal runaway [22] [23]. Thermal runaway is discussed in detail in the next section.

1.2.5.4 Dissolution of current collectors

Over charging and discharging in LIBs results in the dissolution of current collectors such as aluminum metal Al and copper foil Cu [19]. The short circuit in a LIB exists due to the presence of a conductive metal which creates a connection between both electrodes giving rise to a huge current resulting in temperature increase and heat generation triggering the safety problems in LIB. Al and Cu are the conductive metals which can trigger a short circuit in battery after corrosion. The dissolution of Cu occurs at if the battery is over discharged. Cu remains stable at low voltage range but due to over discharge the dissolution of Cu occurs at the anode surface at high potential value.

The current collector for positive electrode is Al, it is stable in air and aqueous solutions. The dissolution of Al occurs due to the passivation of AlF_3 layer on the Al_2O_3 layer of Al collector. This dissolution causes the formation of Al dendrites on anode surface and the corrosion of Al current collector supports the diffusion of fragments of Al within the electrolyte touching both electrode surface. The large-scale corrosion can even lead to the failure of whole battery as it leads to crack formation and degradation of cathode material.

1.3 Thermal Runaway (TR)

Andrey et al. in 2018 presented a review on TR in LIBs [24]. TR occurs with smoke, fire or explosions and it initiates from one cell and propagates to its neighbors causing dangerous consequences at system level [25]. Since 1991 the safety issue associated to the risk of TR is a major problem of lithium batteries. In 2006 the batteries from Dell Lenovo Apple were recalled because of fire and explosions.

1.3.1 Abuse conditions

The conditions for mechanical abuse can be vehicle collision or penetration of the battery pack. The volume expansion of electrode materials may also lead to mechanical abuse. The deformation of battery pack can occur under the effect of external force during a vehicle accident [26][27]. The deformation may result in consequences like:

1. the battery separator breaks causing internal short circuit
2. leakage of electrolyte.

1.3.1.1 Electrical Abuse

Feng et al. reviewed that electrical abuse conditions include external short circuit, overcharge, and over-discharge. The external short circuit can be caused by deformation of battery by improper maintenance, collision, contamination, or water immersion etc [28]. During the state of external short circuit, the battery discharges very fast and the discharging current is high tan the normal state. The external short circuit abuse can be mitigated by use of electronic devices [29]. Balarkrishnan et al. described the use of magnetic switches, fuses, and positive thermal coefficient (PTC) devices to overcome the hazard of external short circuit [20].

Ren et al investigated that overcharge in a battery occurs when the battery is charged above the cut-out voltage and the battery management system fails to function. The TR induced by the overcharge is greater than other abuse conditions as pressure in battery increases [30]. The heat and gas generation occurs during overcharge process which results in the deformation of battery pack and leakage of electrolytes[31]. The author revealed the effect of overcharge with Li ($Ni_xCo_yMn_{1-x-y}$) O2 (NCM)-$Li_yMn_2O_4$ (LMO) cathode material and graphite anode. Transition metal dissolution, phase transition and oxygen gas released at the cathode, whereas, at the anode lithium plating results in deterioration of thermal stability of anode and temperature rise of battery [21].

1.3.1.2 Thermal Abuse

Thermal abuse condition refers to the local overheating and external high temperature. Thermal abuse is caused by loose contacts of the cell connector. Thermal abuse results in separator melting, decomposition of electrodes and finally leads to the TR [32].

1.3.2 Mitigation of TR

The mitigation of TR of lithium-ion battery can be fulfilled in three levels: material level, cell level and system level. The hazards can be reduced by following any of the mitigation strategies discussed here:

1. increasing the intrinsic safety, through modification of materials, to reduce the possibility of abuse conditions [34].
2. Improvement in battery management system, to protect the system before abuse conditions.
3. To mitigate TR after the abuse conditions.

1.3.2.1 Electrolyte

D. D MacNeil et al. in 2000 discussed that electrolyte is a key component in the safety of LIB. Electrolytes such as organic carbonate solvents introduce safety hazards to LIBs due to their flammable nature. Alkyl based solvents react vigorously at elevated temperatures with lithiated graphite and delithiated cathodes (Li_xCoO_2) [39]. The improvement of carbonate-based electrolytes by additives can reduce the safety hazards. Similarly, the development of non-flammable solid state electrolytes, polymers, and room-temperature molten salts (i.e., ionic liquids) can also reduce the flammability of electrolytes.

M Schmidt et al. analyzed the behavior of liquid electrolyte in and investigated a new electrolyte salt which is thermally stable and shows better performance than $LiPF_6$. The paper discusses that $LiPF_6$ used as an electrolyte in lithium-ion cell is thermally unstable and decomposes to LiF and PF_5. The PF_5 hydrolyzes to HF deteriorating the cell performance. To overcome the hydrolyzability of $LiPF_6$ new electrolyte salts known as lithium fluoroalkyl phosphates $LiPF_3(C_2F_5)_3$ were introduced. The resulting salt presents resistance to hydrolysis and has conductivity comparable to $LiPF_6$ [40].

J.-H. Shin et al. presented that room temperature ionic liquids can reduce the safety hazards due to non-flammability and low volatility. The major drawback of ionic liquids is low conductivity. the ionic liquids show conductivity of lithium ions greater than polymer-based electrolytes but are not stable towards reduction in the lithium-ion cell environment [41].

1.3.2.2 Battery management system

Battery management system (BMS) provides protection to the battery operating outside its safe limits. BMS manages different functions, mainly, safe battery operation within specific voltage and temperature interval, thermal management, protection etc. Lithium-ion batteries practically operate under different temperature conditions and the ambient temperature greatly affects the performance of batteries; thus, it is necessary to provide an efficient battery management system [42].

Mohammadian et al. explained that BMS can also be divided into internal thermal management (ITM) and external thermal management (ETM). ITM system, also known as intrinsic safety management, should dissipate heat to avoid the occurrence of over-temperature in a battery cell. The author put forward an internal cooling method in which the electrolyte acts as a coolant and flows through the micro-channels of electrodes [44]. In practical applications ITM method is not efficient due to low cooling efficiency and difficult implementation.

Zheng et al. proposed that ETM system improves heat dissipation form external environment and uses three different kinds of systems i.e., air cooling system (ACS), phase change materials (PCM) cooling system (PCM-CS) and liquid cooling system (LCS) and presented a combined liquid cooling and PCM cooling model, the system showed improved results as it controlled the temperature well in an 8-C battery pack [45].

The BMS and intrinsic safety measures are important for a safe battery system, whereas once the fault occurs countermeasures must be taken like warning and fire extinguishers.

1.4 Problem Statement

The NASICON phase formation is challenging in LATP solid electrolytes. Optimization of sintering temperature is required for perfectly NASICON phase. The secondary phases are always present within the LATP structure such as AlPO4 and Li4P2O7, these phases are present at high sintering temperatures due to the loss of lithium and segregate towards the grain boundary thus blocking the migration channels of lithium ions. The high grain boundary resistance in LATP structure is due to the presence of these impurity phases.

1.5 Objectives

A facile and cost-effective solid-state method was used for synthesis of the NASCION type $Li_{1.3+x+y}Al_{0.3}Y_xTi_{1.7}Si_y(P_{1-y}O_4)_3$ (LAYTSP) (x=0.075 and y=0.4) solid electrolyte. The physiochemical properties were studied by X-ray diffraction (XRD), Scanning electron microscopy (SEM), Fourier-transform infrared spectroscopy (FTIR), X-ray photoelectron spectroscopy (XPS) and electrochemical properties were studied by electrochemical impedance spectroscopy (EIS). The pristine LATP and only Y^{+3} (x=0.775) doped LAYTP electrolytes were also synthesized by the same synthesis method.

Summary

This chapter discuss the background of LIB as an energy storage system and the safety issues associated with the use of LIB in high energy density applications. Thermal runaway is discussed in detail and possible mitigated techniques are mentioned. Further chapter 1 discusses the types and working of solid electrolyte and their performance parameters in detail.

List of References

[1] P. Moriarty and D. Honnery, “What is the global potential for renewable energy?,” *Renew. Sustain. Energy Rev.*, vol. 16, no. 1, pp. 244–252, 2012, doi: 10.1016/j.rser.2011.07.151.

[2] B. Diouf and R. Pode, “Potential of lithium-ion batteries in renewable energy,” *Renew. Energy*, vol. 76, pp. 375–380, 2015, doi: 10.1016/j.renene.2014.11.058.

[3] F. Jia, K. Soucie, S. Alisat, D. Curtin, and M. Pratt, “Are environmental issues moral issues? Moral identity in relation to protecting the natural world,” *J. Environ. Psychol.*, vol. 52, pp. 104–113, 2017, doi: 10.1016/j.jenvp.2017.06.004.

[4] X. Tang, W. Yang, X. Hu, and D. Zhang, “A novel simplified model for torsional vibration analysis of a series-parallel hybrid electric vehicle,” *Mech. Syst. Signal Process.*, vol. 85, pp. 329–338, 2017, doi: 10.1016/j.ymssp.2016.08.020.

[5] T. H. Kim, J. S. Park, S. K. Chang, S. Choi, J. H. Ryu, and H. K. Song, “The current move of lithium ion batteries towards the next phase,” *Adv. Energy Mater.*, vol. 2, no. 7, pp. 860–872, 2012, doi: 10.1002/aenm.201200028.

[6] Y. Sun, “Lithium ion conducting membranes for lithium-air batteries,” *Nano Energy*, vol. 2, no. 5, pp. 801–816, 2013, doi: 10.1016/j.nanoen.2013.02.003.

[7] J. Scheers, S. Fantini, and P. Johansson, “A review of electrolytes for lithium-sulphur batteries,” *J. Power Sources*, vol. 255, pp. 204–218, 2014, doi: 10.1016/j.jpowsour.2014.01.023.

[8] T. Kojima, T. Ishizu, T. Horiba, and M. Yoshikawa, “Development of lithium-ion battery for fuel cell hybrid electric vehicle application,” *J. Power Sources*, vol. 189, no. 1, pp. 859–863, 2009, doi: 10.1016/j.jpowsour.2008.10.082.

[9] G. E. Blomgren, “The Development and Future of Lithium Ion Batteries,” *J. Electrochem. Soc.*, vol. 164, no. 1, pp. A5019–A5025, 2017, doi: 10.1149/2.0251701jes.

[10] K. Kawata, “Industrial success story,” *Chem. Rec.*, vol. 1, pp. 406–413, 2001, [Online]. Available: http://scholar.google.com/scholar?hl=en&btnG=Search&q=intitle:Industrial+Success+Story#5

[11] M. Armand *et al.*, “Lithium-ion batteries – Current state of the art and anticipated developments,” *J. Power Sources*, vol. 479, no. June, 2020, doi: 10.1016/j.jpowsour.2020.228708.

[12] J. Li, C. Daniel, and D. Wood, “Materials processing for lithium-ion batteries,” *J. Power Sources*, vol. 196, no. 5, pp. 2452–2460, 2011, doi: 10.1016/j.jpowsour.2010.11.001.

[13] A. Eftekhari, “Lithium-Ion Batteries with High Rate Capabilities,” *ACS Sustain. Chem. Eng.*, vol.

5, no. 4, pp. 2799–2816, 2017, doi: 10.1021/acssuschemeng.7b00046.

[14] R. Moshtev and B. Johnson, “State of the art of commercial Li ion batteries,” *J. Power Sources*, vol. 91, no. 2, pp. 86–91, 2000, doi: 10.1016/S0378-7753(00)00458-4.

[15] H. Liu, Y. Yang, and J. Zhang, “Reaction mechanism and kinetics of lithium ion battery cathode material LiNiO2 with CO2,” *J. Power Sources*, vol. 173, no. 1, pp. 556–561, 2007, doi: 10.1016/j.jpowsour.2007.04.083.

[16] M. Wakihara, “Recent developments in lithium ion batteries,” *Mater. Sci. Eng. R Reports*, vol. 33, no. 4, pp. 109–134, 2001, doi: 10.1016/S0927-796X(01)00030-4.

[17] J. Wen, Y. Yu, and C. Chen, “A review on lithium-ion batteries safety issues: Existing problems and possible solutions,” *Mater. Express*, vol. 2, no. 3, pp. 197–212, 2012, doi: 10.1166/mex.2012.1075.

[18] R. T. L. Ng and M. H. Hassim, “Strategies for assessing and reducing inherent occupational health hazard and risk based on process information,” *Process Saf. Environ. Prot.*, vol. 97, pp. 91–101, 2015, doi: 10.1016/j.psep.2015.03.014.

[19] D. Ren, X. Feng, L. Lu, X. He, and M. Ouyang, “Overcharge behaviors and failure mechanism of lithium-ion batteries under different test conditions,” *Appl. Energy*, vol. 250, no. April, pp. 323–332, 2019, doi: 10.1016/j.apenergy.2019.05.015.

[20] P. G. Balakrishnan, R. Ramesh, and T. Prem Kumar, “Safety mechanisms in lithium-ion batteries,” *J. Power Sources*, vol. 155, no. 2, pp. 401–414, 2006, doi: 10.1016/j.jpowsour.2005.12.002.

[21] Q. F. Yuan, F. Zhao, W. Wang, Y. Zhao, Z. Liang, and D. Yan, “Overcharge failure investigation of lithium-ion batteries,” *Electrochim. Acta*, vol. 178, pp. 682–688, 2015, doi: 10.1016/j.electacta.2015.07.147.

[22] A. Vassighi and M. Sachdev, “Thermal runaway in integrated circuits,” *IEEE Trans. Device Mater. Reliab.*, vol. 6, no. 2, pp. 300–305, 2006, doi: 10.1109/TDMR.2006.876577.

[23] Q. Wang, P. Ping, X. Zhao, G. Chu, J. Sun, and C. Chen, “Thermal runaway caused fire and explosion of lithium ion battery,” *J. Power Sources*, vol. 208, pp. 210–224, 2012, doi: 10.1016/j.jpowsour.2012.02.038.

[24] X. Feng, M. Ouyang, X. Liu, L. Lu, Y. Xia, and X. He, “Thermal runaway mechanism of lithium ion battery for electric vehicles: A review,” *Energy Storage Mater.*, vol. 10, no. May 2017, pp. 246–267, 2018, doi: 10.1016/j.ensm.2017.05.013.

[25] N. E. Galushkin, N. N. Yazvinskaya, and D. N. Galushkin, “Mechanism of Thermal Runaway in Lithium-Ion Cells,” *J. Electrochem. Soc.*, vol. 165, no. 7, pp. A1303–A1308, 2018, doi: 10.1149/2.0611807jes.

[26] R. Saada, D. Patel, and B. Saha, “Causes and consequences of thermal runaway incidents - Will they ever be avoided?,” *Process Saf. Environ. Prot.*, vol. 97, pp. 109–115, 2015, doi: 10.1016/j.psep.2015.02.005.

[27] L. Huang, Z. Zhang, Z. Wang, L. Zhang, X. Zhu, and D. D. Dorrell, “Thermal runaway behavior during overcharge for large-format Lithium-ion batteries with different packaging patterns,” *J. Energy Storage*, vol. 25, no. June, p. 100811, 2019, doi: 10.1016/j.est.2019.100811.

[28] D. Kong, G. Wang, P. Ping, and J. Wen, “Numerical investigation of thermal runaway behavior of lithium-ion batteries with different battery materials and heating conditions,” *Appl. Therm. Eng.*, vol. 189, no. January, p. 116661, 2021, doi: 10.1016/j.applthermaleng.2021.116661.

[29] X. Feng *et al.*, “Investigating the thermal runaway mechanisms of lithium-ion batteries based on thermal analysis database,” *Appl. Energy*, vol. 246, no. April, pp. 53–64, 2019, doi: 10.1016/j.apenergy.2019.04.009.

[30] D. Ren *et al.*, “A comparative investigation of aging effects on thermal runaway behavior of lithium-ion batteries,” *eTransportation*, vol. 2, p. 100034, 2019, doi: 10.1016/j.etran.2019.100034.

[31] P. Jindal, B. S. Kumar, and J. Bhattacharya, “Coupled electrochemical-abuse-heat-transfer model to predict thermal runaway propagation and mitigation strategy for an EV battery module,” *J. Energy Storage*, vol. 39, no. December 2020, p. 102619, 2021, doi: 10.1016/j.est.2021.102619.

[32] P. Ping, Q. Wang, P. Huang, J. Sun, and C. Chen, “Thermal behaviour analysis of lithium-ion battery at elevated temperature using deconvolution method,” *Appl. Energy*, vol. 129, pp. 261–273, 2014, doi: 10.1016/j.apenergy.2014.04.092.

[33] T. Inoue and K. Mukai, “Roles of positive or negative electrodes in the thermal runaway of lithium-ion batteries: Accelerating rate calorimetry analyses with an all-inclusive microcell,” *Electrochem. commun.*, vol. 77, pp. 28–31, 2017, doi: 10.1016/j.elecom.2017.02.008.

[34] S. Wilke, B. Schweitzer, S. Khateeb, and S. Al-Hallaj, “Preventing thermal runaway propagation in lithium ion battery packs using a phase change composite material: An experimental study,” *J. Power Sources*, vol. 340, pp. 51–59, 2017, doi: 10.1016/j.jpowsour.2016.11.018.

[35] X. Feng, D. Ren, X. He, and M. Ouyang, “Mitigating Thermal Runaway of Lithium-Ion Batteries,” *Joule*, vol. 4, no. 4, pp. 743–770, 2020, doi: 10.1016/j.joule.2020.02.010.

[36] Y. Bai, Q. Chang, Q. Yu, S. Zhao, and K. Jiang, "A novel approach to improve the electrochemical performances of layered LiNi1/3Co1/3Mn1/3O2 cathode by YPO4 surface coating," *Electrochim. Acta*, vol. 112, pp. 414–421, 2013, doi: 10.1016/j.electacta.2013.09.002.

[37] P. Guan *et al.*, "Recent progress of surface coating on cathode materials for high-performance lithium-ion batteries," *J. Energy Chem.*, vol. 43, pp. 220–235, 2020, doi: 10.1016/j.jechem.2019.08.022.

[38] R. EL Khalfaouy *et al.*, "Nickel-substituted LiMnPO4/C olivine cathode material: Combustion synthesis, characterization and electrochemical performances," *Ceram. Int.*, vol. 45, no. 14, pp. 17688–17695, 2019, doi: 10.1016/j.ceramint.2019.05.336.

[39] D. D. MacNeil, D. Larcher, and J. R. Dahn, "Comparison of the Reactivity of Various Carbon Electrode Materials with Electrolyte at Elevated Temperature," *J. Electrochem. Soc.*, vol. 146, no. 10, pp. 3596–3602, 1999, doi: 10.1149/1.1392520.

[40] M. Schmidt *et al.*, "Lithium fluoroalkylphosphates: A new class of conducting salts for electrolytes for high energy lithium-ion batteries," *J. Power Sources*, vol. 97–98, pp. 557–560, 2001, doi: 10.1016/S0378-7753(01)00640-1.

[41] J. H. Shin, W. A. Henderson, and S. Passerini, "Ionic liquids to the rescue? Overcoming the ionic conductivity limitations of polymer electrolytes," *Electrochem. commun.*, vol. 5, no. 12, pp. 1016–1020, 2003, doi: 10.1016/j.elecom.2003.09.017.

[42] Q. Li *et al.*, "Numerical investigation of thermal runaway mitigation through a passive thermal management system," *J. Power Sources*, vol. 429, no. April, pp. 80–88, 2019, doi: 10.1016/j.jpowsour.2019.04.091.

[43] D. Ouyang, M. Chen, Q. Huang, J. Weng, Z. Wang, and J. Wang, "A Review on the thermal hazards of the lithium-ion battery and the corresponding countermeasures," *Appl. Sci.*, vol. 9, no. 12, 2019, doi: 10.3390/app9122483.

[44] S. K. Mohammadian, Y. L. He, and Y. Zhang, "Internal cooling of a lithium-ion battery using electrolyte as coolant through microchannels embedded inside the electrodes," *J. Power Sources*, vol. 293, pp. 458–466, 2015, doi: 10.1016/j.jpowsour.2015.05.055.

Chapter: 2 Literature Review

2.1 Solid electrolyte

Solid electrolytes are also known as superfast ionic conductors, they exhibit the ionic conductivity comparable with liquid electrolytes i.e., > 10^{-2} S/cm at room temperature. Solid electrolytes are ionic conductors, and their electronic conductivity is negligible. These electrolytes on one hand can eliminate the flammability and leakage problems associated with liquid electrolytes but also reduce the formation of lithium dendrites and improve the performance of the battery. Solid electrolyte is the key component in all solid-state lithium batteries (ASSLBs) [1]. Having a greater energy density than ordinary metal ion batteries, advanced ASSLBs are widely regarded as the most promising future technology of energy storage technology. ASSLBs are promising devices when compared with conventional energy storage devices in terms of energy density, compactness, stability, and safety [2].

2.1.1 Brief History of ASSLBs

The first solid state battery was developed in 1950 incorporating silver based solid ionic conductor. The internal resistance if the battery was very high with low current density. Silver was also used as anode material, the electrochemical performance of battery was very low however, it exhibited a great mechanical strength and a loner shelf life. In 1990 Oak Ridge National Laboratory developed a latest version of solid-state battery afterwards transforming it into thin film LIB [3]. In 2003 the university of Colorado Boulder developed a high energy density ASSLB with composite cathode material [4]. In 2004 Dyson Ltd produced a commercial high energy density ASSLB. Similarly, in 2017 new ASSLB was manufactured using a glass electrolyte and metal anode based on alkali metals (Li^+, Na^+ and K^+) [5].

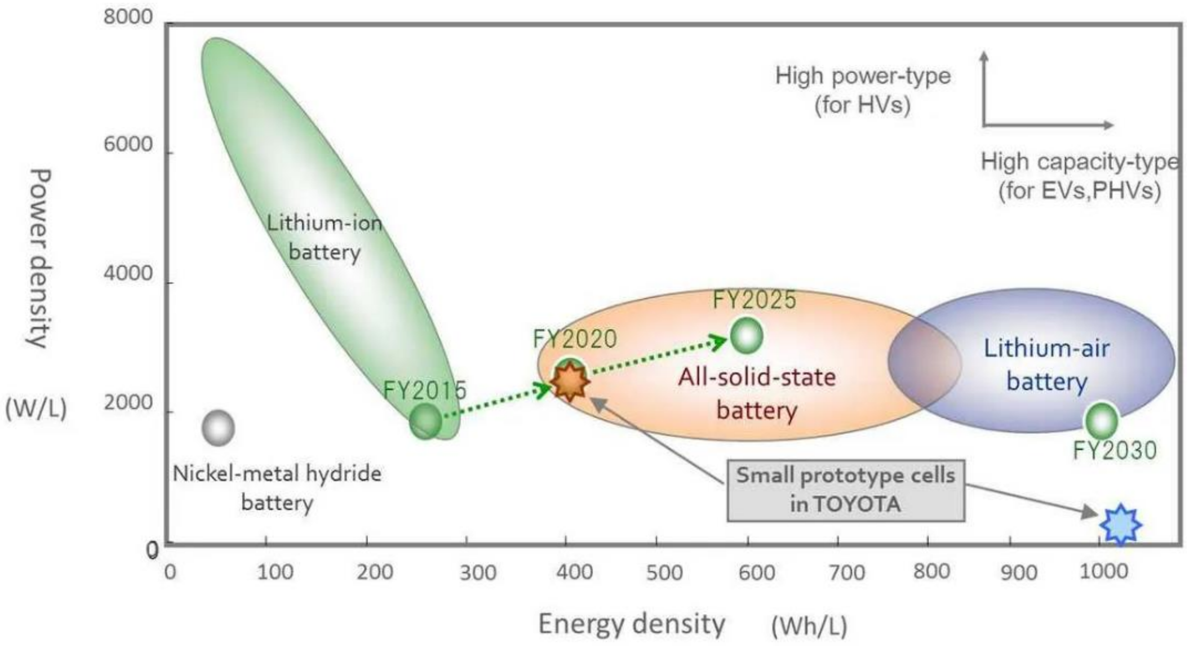

Figure 2.1: Ragone plot of different battery systems

2.1.2 Types of Solid electrolytes

Solid electrolytes are classified into polymer, inorganic, and composite electrolytes. Polymer electrolytes include PVF poly (vinylidene fluoride), PMM poly (methyl methacrylate) and PEO poly (ethylene oxide) based electrolytes[6],[7], inorganic solid electrolytes include sulfides and oxides-based electrolytes, and composites are synthesized using both polymer and ceramic materials[8],[9]. Oxide based electrolytes are highly stable in air and moisture whereas sulfide-based electrolytes are unstable in air and require extra handling[10],[11],[12],[13]. Because of their properties numerous efforts have been devoted to the development of oxide based solid ionic conductors, including NASICON type, LISICON-like sulfide electrolytes[14], perovskites and garnet-based LLTO and LLZO electrolytes[15],[16].

Table 2.1: Types of Solid electrolytes

Solid electrolytes				**References**
Organic electrolytes	Solid polymer electrolytes	Polymer matrix incorporating inorganic fillers	Passive fillers and Active fillers	[22, 23, 25, 26] and [27, 28, 29]
		Polymer filled 3D framework	3D framework incorporating inorganic electrolyte solutions	[30, 31]
		Composite electrolytes with open framework	Metal organic framework (MOF) filler incorporated polymer matrix	[36]
		Layered structures	The polymer layer acts as an interface between electrodes and electrolyte.	[38, 39]
Inorganic electrolytes	Oxide solid electrolytes	Garnet	Empirical formula: $Li_3Ln_3M_2O_{12}$	[9], [15], [12], [41]
		Perovskites	$Li_{3-x}La_{2/3-x}TiO_3$	[42, 43, 45]
		LISICON	$Li_{1.4}Zn\ (GeO_4)_4$	[14], [50, 51]
		LIPON	Li_3PO_4	[52, 53, 55, 56]
		NASICON	General formula: $NaM_2(PO_4)_3$	[50, 57, 59]

2.2 Solid Polymer Electrolytes

Solid polymer electrolytes incorporate salts of lithium in polymer materials. Polyethylene oxide (PEO) is the first and most studied material to incorporate lithium metal salt. The liquid host is not suitable for addition in PEO making it free form leakage. Although the polymer electrolyte materials are flexible, safe, and compatible however, the ionic conductivity of these electrolytes is very low in range of 10^{-6}-10^{-8} S/cm, poor mechanical strength and dendrite growth limit their use in ASSLBs [18]. In order to overcome these limitations in many studies the combination of polymers and other material is reported which resulted in improved performance. This new form of electrolytes is called composite solid-state electrolytes (CSSEs) and are considered as the solid electrolytes for future ASSLBs. CSSEs are divided into three types [20]

1. Inorganic- organic
2. Organic-organic
3. Inorganic-inorganic.

Among these the inorganic/polymer are the most promising and widely investigated electrolytes. The following structure of CSSEs are used in LIBs

- Polymer matrix incorporating inorganic fillers
- Polymer filled inorganic 3D framework
- Composite electrolytes with open framework
- Layered structures

2.2.1 Polymer matrix incorporating inorganic fillers

The inorganic fillers are divided into two types depending on their ionic conductivities i.e., active fillers and passive fillers [20]. The active have high ionic conductivities and large Li^+ transference numbers however, their synthesis is quite difficult, and they are not easily tunable with polymer matrix. Active fillers are moisture and CO_2 sensitive. The passive fillers are inexpensive, easy to handle and tunable in matrix however, they offer low conductivities, and the interfacial resistance is very high [21].

2.2.1.1 Passive fillers

To increase the electrochemical performance, mechanical strength, and thermal stability the incorporation of passive fillers in polymer matrix is the most widely studied CSSEs. The passive fillers are divided into two types i.e., metal and non-metal oxide fillers. The former fillers include silicon dioxide $SiO_{2,}$ aluminum oxide Al_2O_3, titanium oxide TiO_2 [22]and zirconium oxide ZrO_2 etc. The conductivity Al_2O_3 remains almost same however the mechanical strength of the electrolyte increase [23]. In case of TiO_2 the transference number of lithium ions increase resulting in high ionic conductivity [24].

Carbon is the non-metal oxide filler, although carbon is an anode material not an electrolyte material, but the incorporation of small portion of carbon in PEO matrix resulted in high ionic conductivity and large surface area [25]. The other non-metal fillers utilized are sand, clay, zeolite, and nonporous materials. Agglomeration occurs while addition of metal oxide fillers in polymer matrix by further increasing the filler content ration does not affect the ionic conductivity of composites. The replacement of 0D metal oxide filler by 1D filler can reduce the formation of agglomerates by providing a longer dimension [26].

2.2.1.2 Active fillers

Active fillers offer high ionic conductivities compared to passive fillers and more filler content can be added in matrix rather than passive filler in which by increasing the fraction ratio of filler the interface area increases but the ionic conductivity decreases [27]. Gallium based garnet electrolyte Ga-LLZO immersed in a polymer matrix create a space charge region which results in high ionic conductivity. This region generates due to the defects already present on the Ga-LLZO surface. The one- and two-dimensional active fillers are prepared by template solution method. Different synthesis methods are employed for incorporating these fillers in polymer matrices [28]. Electrospinning method is used by Liu et al. to prepare CSSE by calcination of PVP fibers which contain the precursors of perovskites LLTO electrolyte. The vacancies in the structure promote the hopping of Li^+ ions thus increasing the ionic conductivity [29].

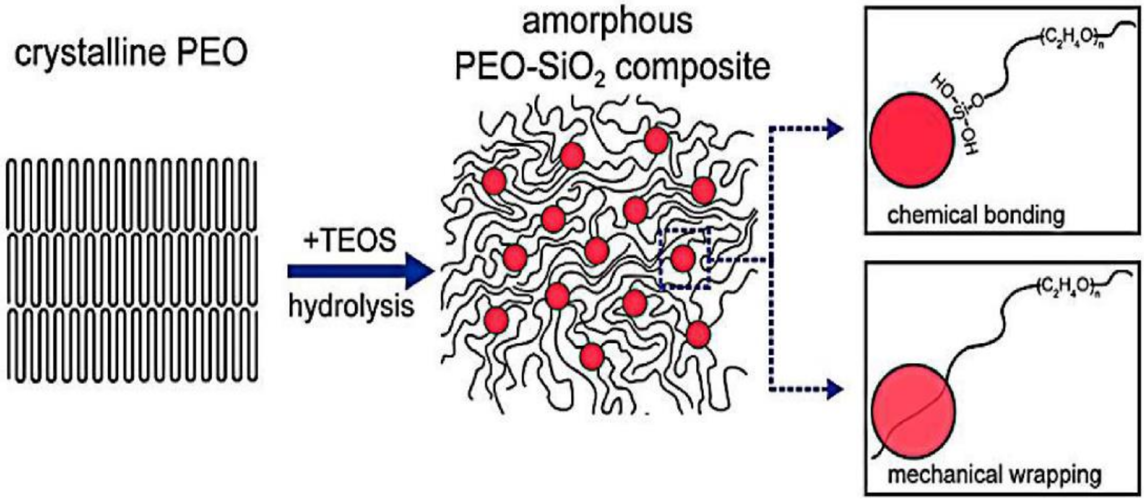

Figure 2.2: Schematic diagram of incoporation of SiO_2 in PEO matrix

2.2.2 Polymer filled 3D framework

The incorporation of fillers in polymer matrix reduces the crystal formation in polymeric chain resulting in high ionic conductivity. Many researchers are now working on the inorganic fibers and rods to increase the electrochemical performance [26]. Recently, polymer filled 3D inorganic frameworks have been developed that provides more free channels for lithium ion hopping than nanorods and wires [30]. These frameworks are prepared by sol-gel method and heat treatments. A continuous 3D framework has been prepared by J. Bae et al. of inorganic LLTO structure by sol-gel method, the polymer was added afterwards in the framework. The respective ionic conductivity was in the range of 8.8×10^{-5} S/cm at room temperature [31].

2.2.3 Composite electrolytes with open framework

Metal oxide framework (MOFs) are multi-dimensional materials composed of metal centers connected by organic linkers. There may be several thousand square meters per gramme of surface area in some of these MOFs because of the development of void spaces within the coordination network of the organic molecules [32]. They are recently used in electrochemical systems as catalysts, electrode materials and electrolytes [33]. Fleker et al. synthesized MOF-activated carbon compositions to talk about nonconductive nature of MOFs, a result of the network's coordinating bonds. MOF nanoparticles in contact with activated carbon show an interesting EPR signal [34]. The MOF's Cu^{2+}/Cu^{+} redox couple increases the AC's double-layer capacitance by 30 percent. Yaghi et al. conducted a comprehensive study on the growth of MOF on graphene sets. Zirconium-MOF showed an aerial capacitance of 5.09 μF/cm for over 10,000 charge/discharge cycles [35].

In case of CSSEs the MOFs exits in the form of polymer matrix dipped with MOF fillers mixed with Li salts. H. Huo et al developed a MOF filler incorporated PEO with LiTFSi based polymer matrix and a cell incorporating this SSE. The electrolyte showed a high ionic conductivity of 3.65×10^{-5} S/cm which is higher than the pristine electrolyte compound. Research work has been done on this type of CSSEs widely on Mg- tissue plasminogen activator (TPA) and Al-TPA-MOF [36].

2.2.4 Layered structures

The layered structure of CSSEs includes inorganic fillers in polymer matrix and it provides a flexible structure and ability to detect the advantages and disadvantages of lithium ion hopping in each layer. These structures not only increase the ionic conductivity and mechanical strength but also enhance the interfacial contact between electrode/electrolyte surface [37]. The layered structures are mainly divided into double layered and sandwich structure based on the work of a group of scientists.

In double layered structure the polymer layer acts as a solid interface layer and is present between the inorganic pellet and Li metal anode [38]. This layer as described in figure reduces the dendrite growth and reduces the interfacial resistance between the contacts. In the sandwich structure electrolyte, the soft interface of polymer is used between both electrodes and the electrolyte. W. Zhou synthesized a CSSE with a ceramic layer ($L_{1.3}Al_{0.3}Ti_{1.7}(PO_4)_3$) sandwiched between two polymer layers (PEO and PEMA) and resulted in a decrease in interfacial contact [39].

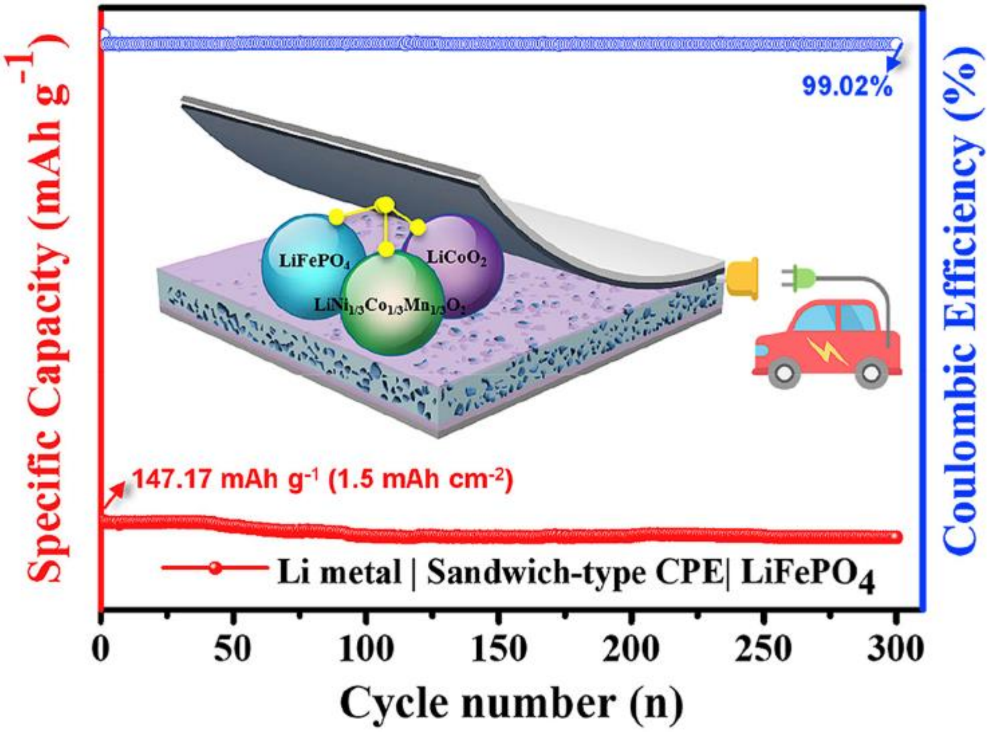

Figure 2.3: Sandwich type of CSSE.

2.3 Inorganic Electrolytes

Inorganic electrolytes are also known as ceramic electrolytes have lithium-ion conduction ability and these electrolytes mainly include amorphous (glass) and crystalline structures. Among SSEs the inorganic has high ionic conductivities and thermal stability. The transference number of Li ions in inorganics is almost unity and they are also called single ion conductors. The ion conduction in ceramics occur through vacancies and interstitial sites compared to liquid electrolytes [2]. The inorganic solid electrolytes are divided into oxides and sulfides. The disadvantages of some ceramics include poor contact with cathode material and low ionic conductivity which limits further research on them for example lithium halides and lithium hydrides [1].

The most concerning property of ceramics of electrochemical and thermal stability. Although they possess high ionic conductivities and wide voltage window still some are not stable at high temperatures. These unstable ceramics result in dendrite growth, low electrochemical performance, and decomposition. Solid electrode interface (SEI) layer is formed due to the decomposition of electrolyte which results in increase in voltage window. Cell aging is cause by this SEI layer [40].

2.4 Oxide based SEs

The oxide-based electrolyte includes garnet type, perovskite, LISICON and NASICON type structures.

2.4.1 Garnet-type structures

In 1968 the first garnet type structure was synthesized with formula $Li_3Ln_3M_2O_{12}$ where Ln= Yb, Lu, Gd, Y, Nd, Tm, Tb and M=W, Te. With Te in the structure the lattice parameters are changed by the ionic radius of elements added at Ln site [41]. Stable TeO_6 octahedral are formed in $Li_3Ln_3Te_2O_{12}$ which further allow the addition of vast range of elements at Ln site whereas with W element at M site the octahedral formed within $Li_3Ln_3W_2O_{12}$ structure is unstable and only limited cations can be added [12]. Thangadurai et al. reported a new garnet structure with Nb and Ta at M site and La at Ln site. High ionic conductivity in range 10^{-6} S/cm was reported at room temperature. $Li_3La_3Nb_2O_{12}$ has high ionic conductivity than Ta doped element however $Li_3La_3Ta_2O_{12}$ is more stable with Li metal because of its low reduction potential. These compounds have a 3D framework for diffusion of lithium ions [13].

Different modifications in garnet structure have been made by doping strategy. Ba doped $Li_3La_3Ta_2O_{12}$ showed high ionic conductivity and it was equal to bulk conductivity~4×10^{-5} S/cm at room temperature [9]. Similarly, $Li_3SrLa_3Ta_2O_{12}$ oxide also represented a high ionic conductivity and is found to be superior to other oxide-based electrolytes. Murugan et al. synthesized a new SSE by completely replacing Ta by zirconium Zr $Li_7La_3Zr_2O_{12}$ which presented 3×10^{-4} S/cm ionic conductivity at room temperature with a cubic structure [42]. LLTO structure contains octahedrons with Li ions occupancies and 67.9% of these are displaced. Niobium and zirconium do-doped LLTO structure shows an ionic conductivity of 8×10^{-4} S/cm at room temperature and it was found that bulk conductivity was less than the total ionic conductivity. The voltage window was reported 0-9 V with 90% capacity of ASSLB prepared with lithium cobalt cathode and lithium metal anode [15].

The garnet type electrolyte is moisture and CO_2 sensitive. Recently research is conducted to stabilize the LLZO garnet.

2.4.2 Perovskite SSE

The first perovskite SE was prepared by Inaguma et al. with general formula $Li_{3-x}La_{2/3-x}TiO_3$ (LLTO) it represented a total ionic conductivity of 2×10^{-5} S/cm and bulk ionic conductivity of 1×10^{-3} S/cm at room temperature [43]. LLTO crystal structure consists of Li and La ions at A sites and Ti ions at B site. Oxygen ions create potential barriers and Li ions migrate from one A site to ither within the structure, by enlarging the lattice parameters the size bottlenecks can be changed. Inaguma et al. prepared an SSE by doping 5% molar ration of Sr at A site of LLTO. It increased the lattice parameters thus the bottleneck size was increased, and total ionic conductivity was also increased. However, it was found that the Sr doping resulted in decrease in number of Li ions when the doping concentration of Sr was higher than 0.1 [44].

The grain boundary resistance of LLTO was higher despite the low resistance in bulk of the magnitude 10^{-5} S/cm at room temperature and resulted in high total resistance. LLTO was found to be unstable at low 1.8 V voltage level and was incompatible with lithium metal anode. The low stability in the structure was caused by Ti^{+4} as it reduces at low voltage [45]. To work on this issue Chung et al. doped Ti site with Sn^{+4}, Zr^{+4}, Mn^{+4} and Ge^{+4}. The ionic conductivity improved in case of Mn and Ge, to avoid impurity phase formation Ti was only substituted not replaced entirely however the remaining Ti was still able to reduce [46]. Thangaduari et al. synthesized Sr and Zr doped LTO structure, it was stable with lithium metal because of the oxidation states of Zr and Ta [47]. The ionic conductivity was low, to improve the conductivity Cheng et al. synthesized $Li_{3/8}$ $Sr_{7/16}$ $Ta_{3/4}$ $Zr_{1/4}$ O3 (LSTZ) changing the concentration in the pristine SSE and the ionic conductivity was found to be 2×10^{-4}S/cm. LSTZ was found to be stable at low voltage levels and its grain conductivity was higher than LLTO SSE [45].

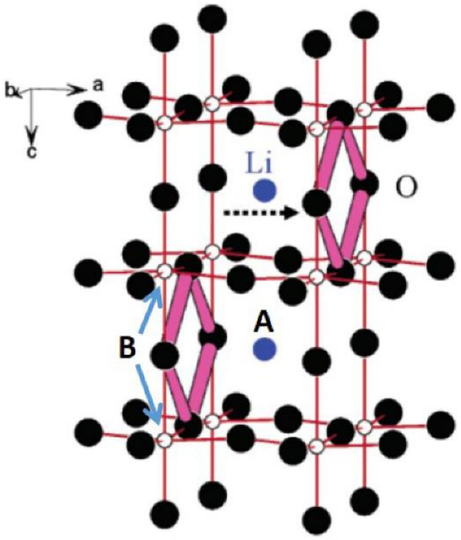

Figure 2.4: Structure of perovskite LLTO

2.4.3 LISICON

Lithium superionic conductor (LISICON) was first reported by Hong et al. the electrolyte $Li_{1.4}Zn$ $(GeO_4)_4$ presented the ionic conductivity 1.25×10^{-1} S/cm at temperature above 100 °C [49]. Li ion conduction depended upon two factors: bonding energy and size of channels. In this structure the network is formed by $[Li_{1.1}Zn\ (GeO_4)]^{-3}$ and the remaining three Li ions can move freely. The O^{-2} bonds strongly with Li, Zn and Ge and creates weak bonds with three Li ions. The Li ions move freely in only two directions because of the shape of channels in parallelogram form. These ions are present in 4c and 4a position within the structure and can diffuse through vacancies and interstitial atoms thus improving the ionic conductivity. However, the ionic conductivity of this LISICON SSE was very low and it is further studied [50].

Hue et al. performed a synthesis to create three solid solutions between lithium orthosilicate, lithium phosphate and $Li_{4-x}Si_{1-x}$ P_xO_4. The highest ionic conductivity was found at x=0.5 and x=0,4 concentration of 10^{-6} S/cm, the substitution of cation Si with phosphorus ion interstitial lithium ions were introduced [51]. However, a structural change occurred at these concentrations. $Li_{10.42}Si_{1.5}$ $P_{.5}Cl_{0.08}O_{11.92}$ and $Li_{10.42}Ge_{1.5}$ $P_{.5}Cl_{0.08}O_{11.92}$ electrolytes were synthesized by Song et al. partially doped oxygen O^{-1} and chlorine Cl^{-1} and achieved ionic conductivities of 1.03×10^{-5} S/cm and 3.7×10^{-5} S/cm. due to large size of Cl^{-1} the lattice volume of channels increases, the bonding between Li and Cl is weaker therefor releasing Li ions for conduction [14].

LISICON have not been utilized in ASSLBs due to low ionic conductivities. The presence of O^{-2} in the structure creates strong bond with lithium so by replacing it by S^{-2} can increase the ionic conductivity as reported by Kamaya et al.

2.4.4 LIPON

Lithium phosphorus oxynitride (LIPON) is an amorphous SSE. The first electrolyte was synthesized by Bates et al. by magnetron sputter on lithium phosphate surface in nitrogen atmosphere. The ionic conductivity was in range of 2×10^{-6} S/cm RT and provided a stable interface with lithium metal [52]. Suzuki et al used the same synthesis method and but changed the target to combination of lithium phosphate and lithium oxide with molar ratio 1:2. The ionic conductivity was three times higher than the pristine material. The conductivity increased due to the increase of Li ions however the further increase led to a decrease in ionic conductivity due to decreased ion phosphate chains which promote Li ion conduction [53]. Ion beam assisted deposition method was used by Li et al. for deposition of N_2 and the flow was controlled by mixture of nitrogen and argon in molar ratio 1:8. The ionic conductivity was found to be 4.5×10^{-6} S/cm at 25 ℃ [54]. Su et al. and Fujibayashi et al. prepared LiPON films with RF sputtering and chemical vapor deposition respectively. The ionic conductivity was found to be 4.9×10^{-6} S/cm and 5.3×10^{-6} S/cm for thickness films 190nm and 95 nm [55].

Van Jodin et al. prepared the electrolyte films by magnetron and non-magnetron sputter coating; the ionic conductivity was found to be 1.4×10^{-6} S/cm and 6.7×10^{-6} S/cm at RT. In the first type only PO_4^{-3} group was detected, in second type PO_3^{-2} and PO_2^{-1} groups were observed. These groups create disorder in the structure leading to mobile Li ions thus increasing the conductivity [56]. In a LiPON based battery the cathode, electrolyte, current collectors, and anode were deposited to form thin films and coating was used to prevent Li metal contact with air. LiPON can be incorporate din thin films-based batteries however they are not suitable for ASSLBs.

2.4.5 NASICON

Sodium super ion conductor (NASICON) with the general formula $NaM_2(PO_4)_3$ where M positive ion. One of the examples of such system is $Na_{1+x}Zr_2Si_xP_{3-x}O_{12}$ (x=0-3). NASICON has rhombohedral structure in range 0:3, while it exhibits a completely different structure in range x=1.8: 2.2, monoclinic structure. Figure shows a 3D framework and pathways in which PO_4 and SiO_4 tetrahedrons relate to ZrO_6 octahedrons by sharing Oxygen atoms within. Sodium Na ions are present at A1 site and jump between A1 and A2 sites then diffuse along c axis. A1 sites are occupied only when x=0 and the energy for the transport of mobile ions is higher, when x>0 the activation energy decrease as spare mobile ions occupy A1 sites [57]. The size of the ions determines the size of pathways and diffusion of ions also depends on pathways. In contrast the diameter of pathways than two times the sum of radius of Na ions and O ions. To enhance the ionic conductivity the framework ions should be considered according to Na ions radius. SSE $Na_3Zr_2Si_2PO_{12}$ was synthesized having monoclinic structure and demonstrated the conductivity of 2×10^{-1} S/cm at high temperatures [58].

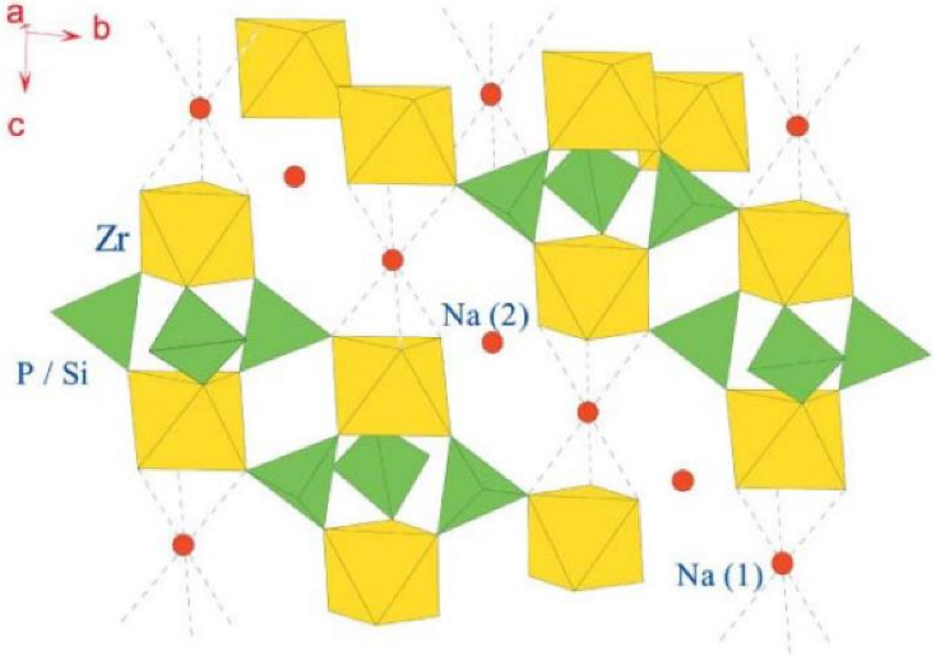

Figure 2.5: NASICON crystal structure

$LiZr_2(PO_4)_3$ electrolyte is prepared by placing Li ions instead of Na ions, the electrolyte demonstrated a monoclinic phase when prepared at 1200℃ and ionic conductivity of 3.3×10^{-6} S/cm very less than its Na counterpart [59]. Due to high temperature the phase changed from monoclinic to rhombohedral at 40 ℃ and presented a high ionic conductivity of 1.2×10^{-2} S/cm at high temperatures. The synthesis at low temperature also exhibited a phase change from monoclinic to orthorhombic. Aono et al. reported $LiM_2(PO_4)_3$ with M= Ge, Hf and Ti, the Ti doped (LTP) NASICON type SSE presented a high ionic conductivity most stable structure for lithium-ion conduction among other dopants [50]. Further substituting trivalent cations Al^{+3} and Fe^{+3} in M^{+4} site introduces vacancies and hence increases the electrochemical performance in $Li_{1+x}Fe_xHf_{2-x}(PO_4)_3$, $Li_{1+x}Al_xTi_{2-x}(PO_4)_3$ (LATP) and $Li_{1+x}Al_xGe_{2-x}(PO_4)_3$(LAGP). The ionic conductivity is greater than 10^{-4} S/cm, among these three structure $Li_{1.3}Al_{0.3}Ti_{1.7}(PO_4)_3$ displayed the highest conductivity of 7×10^{-4} S/cm at room temperature, but Ti^{+4} reduces in the structure resulting in low stability. Therefore, $Li_{1+x}Fe_xHf_{2-x}(PO_4)_3$ and $Li_{1+x}Al_xGe_{2-x}(PO_4)_3$ demonstrates good stability [60]. The doping of lithium phosphate Li_3PO_4 and lithium borate Li_3BO_3 produces dense electrolytes with conductivity of 3×10^{-4} S/cm for LTP-0.2Li_3BO_3 [61].

Two types of NASICON type SSE are widely studied LATP and LAGP SSE. LATP NASICON represents high ionic conductivity however it suffers from incompatibility with electrode material especially lithium metal as anode due to the reduction if Ti^{+4}. Lithium addition in LTP was conducted to work on this issue and two electrolytes were synthesized LTP and $Li_3Ti_2(PO_4)_3$ both exhibiting rhombohedral structures however the Li ion distribution was different in both. In LTP lithium is present at A1 site and A2 site is empty whereas in $Li_3Ti_2(PO_4)_3$ the lithium occupied A2 site and A1 site was empty [62]. This distribution resulted in an increase in c axis and the repulsions with octahedrons also increased.

LAGP electrolyte was first developed by melt quenching method to form. The reported ionic conductivity was 4×10^{-4} S/cm at 25 ℃ [63]. The conductivity enhanced as in glass the structure is dense and close contact exits between the grains. Another scientist added Li_2O in the $Li_{1+x}Al_xGe_{2-x}(PO_4)_3$ LAGP structure for x=0.5. Secondary phases of lithium were formed which helped in crystallization of glass and hence improved the conductivity, the grain and total conductivity values were 1.18×10^{-3} S/cm and 7.25×10^{-4} S/cm at RT [64]. The electrochemical and thermal stability was excellent, and the electrolyte was stable at 6 V. higher temperature sintering showed high ionic conductivities however, when the temperature was increased above 900 ℃ another impurity phase $AlPO_4$ was formed that reacted with lithium and decreased the number of mobile lithium ions thus affecting the conductivity[65].

Among NASICON SSEs LAGP shows high ionic conductivity, wide voltage window and excellent electrochemical stability. However, its application in ASSLBs is limited due to expensive raw material GeO_2 used in the synthesis [66]. The replacement of germanium with cheap material can make this electrolyte applicable for utilization in ASSLBs.

Summary

This chapter consists of the literature review on the types of electrolyte materials used for ASSLBs. In addition, the performance of the solid-state electrolytes is also discussed in the chapter. Moreover, this chapter also contains the benefits and shortcomings of oxide-based electrolyte derived materials for the energy storage applications.

List of References

[1] E. Quartarone and P. Mustarelli, “Electrolytes for solid-state lithium rechargeable batteries: Recent advances and perspectives,” *Chem. Soc. Rev.*, vol. 40, no. 5, pp. 2525–2540, 2011, doi: 10.1039/c0cs00081g.

[2] R. Chen, W. Qu, X. Guo, L. Li, and F. Wu, “The pursuit of solid-state electrolytes for lithium batteries: From comprehensive insight to emerging horizons,” *Mater. Horizons*, vol. 3, no. 6, pp. 487–516, 2016, doi: 10.1039/C6MH00218H.

[3] A. Yoshino, *Development of the Lithium-Ion Battery and Recent Technological Trends*. Elsevier, 2014. doi: 10.1016/B978-0-444-59513-3.00001-7.

[4] Y. Liu, R. Zhang, J. Wang, and Y. Wang, “Current and future lithium-ion battery manufacturing,” *iScience*, vol. 24, no. 4, p. 102332, 2021, doi: 10.1016/j.isci.2021.102332.

[5] A. Eftekhari, “Lithium-Ion Batteries with High Rate Capabilities,” *ACS Sustain. Chem. Eng.*, vol. 5, no. 4, pp. 2799–2816, 2017, doi: 10.1021/acssuschemeng.7b00046.

[6] L. Yue *et al.*, “All solid-state polymer electrolytes for high-performance lithium ion batteries,” *Energy Storage Mater.*, vol. 5, pp. 139–164, 2016, doi: 10.1016/j.ensm.2016.07.003.

[7] Y. Zhao *et al.*, “A new solid polymer electrolyte incorporating Li 10 GeP 2 S 12 into a polyethylene oxide matrix for all-solid-state lithium batteries,” vol. 301, pp. 47–53, 2016, doi: 10.1016/j.jpowsour.2015.09.111.

[8] W. Xiao *et al.*, “High performance composite polymer electrolytes doped with spherical-like and honeycomb structural Li0.1Ca0.9TiO3 particles,” *Front. Chem.*, vol. 6, no. OCT, pp. 1–10, 2018, doi: 10.3389/fchem.2018.00525.

[9] J. Bae *et al.*, “A 3D Nanostructured Hydrogel-Framework-Derived High-Performance Composite Polymer Lithium-Ion Electrolyte,” *Angew. Chemie - Int. Ed.*, vol. 57, no. 8, pp. 2096–2100, 2018, doi: 10.1002/anie.201710841.

[10] S. Chen *et al.*, “Sulfide solid electrolytes for all-solid-state lithium batteries: Structure, conductivity, stability and application,” *Energy Storage Mater.*, vol. 14, no. February, pp.

58–74, 2018, doi: 10.1016/j.ensm.2018.02.020.

[11] Y. Sun, K. Suzuki, S. Hori, M. Hirayama, and R. Kanno, “Superionic Conductors: Li10+δ[SnySi1-y]1+δP2-δS12 with a Li10GeP2S12-type Structure in the Li3PS4-Li4SnS4-Li4SiS4 Quasi-ternary System,” *Chem. Mater.*, vol. 29, no. 14, pp. 5858–5864, 2017, doi: 10.1021/acs.chemmater.7b00886.

[12] Z. Wang, J. Mo, Y. Wu, H. Ye, and X. Wu, “Synthesis of lithium garnet oxides of the compositions series Li7-xLa3Zr2-xTaxO12,” *J. Wuhan Univ. Technol. Mater. Sci. Ed.*, vol. 32, no. 6, pp. 1261–1264, 2017, doi: 10.1007/s11595-017-1739-y.

[13] L. Shen *et al.*, “Preparation and characterization of Ga and Sr co-doped Li7La3Zr2O12 garnet-type solid electrolyte,” *Solid State Ionics*, vol. 339, no. May, p. 114992, 2019, doi: 10.1016/j.ssi.2019.05.027.

[14] M. Murayama, N. Sonoyama, A. Yamada, and R. Kanno, “Material design of new lithium ionic conductor, thio-LISICON, in the Li2S-P2S5 system,” *Solid State Ionics*, vol. 170, no. 3–4, pp. 173–180, 2004, doi: 10.1016/j.ssi.2004.02.025.

[15] C. Shao, Z. Yu, H. Liu, Z. Zheng, N. Sun, and C. Diao, “Enhanced ionic conductivity of titanium doped Li7La3Zr2O12 solid electrolyte,” *Electrochim. Acta*, vol. 225, pp. 345–349, 2017, doi: 10.1016/j.electacta.2016.12.140.

[16] J. C. Bachman *et al.*, “Inorganic Solid-State Electrolytes for Lithium Batteries: Mechanisms and Properties Governing Ion Conduction,” *Chem. Rev.*, vol. 116, no. 1, pp. 140–162, 2016, doi: 10.1021/acs.chemrev.5b00563.

[17] Y. Zheng *et al.*, “A review of composite solid-state electrolytes for lithium batteries: Fundamentals, key materials and advanced structures,” *Chem. Soc. Rev.*, vol. 49, no. 23, pp. 8790–8839, 2020, doi: 10.1039/d0cs00305k.

[18] R. C. Agrawal and G. P. Pandey, “Solid polymer electrolytes: Materials designing and all-solid-state battery applications: An overview,” *J. Phys. D. Appl. Phys.*, vol. 41, no. 22, 2008, doi: 10.1088/0022-3727/41/22/223001.

[19] L. C. Charles Hardy and D. F. Shriver, “Preparation and Electrical Response of Solid Polymer Electrolytes with Only One Mobile Species,” *J. Am. Chem. Soc.*, vol. 107, no. 13, pp. 3823–3828, 1985, doi: 10.1021/ja00299a012.

[20] K. Murata, S. Izuchi, and Y. Yoshihisa, “Overview of the research and development of solid polymer electrolyte batteries,” *Electrochim. Acta*, vol. 45, no. 8, pp. 1501–1508, 2000, doi: 10.1016/S0013-4686(99)00365-5.

[21] F. Deng *et al.*, “Microporous polymer electrolyte based on PVDF/PEO star polymer blends for lithium ion batteries,” *J. Memb. Sci.*, vol. 491, pp. 82–89, 2015, doi: 10.1016/j.memsci.2015.05.021.

[22] A. Bhaskar, J. J. Yuan, and C. J. Liu, “The effects of Si doping on the thermoelectric and magnetic properties of Ca0.98Bi0.02Mn1-xSixO 3-δ with x = 0.00, 0.02 and 0.03,” *Mater. Sci. Eng. B Solid-State Mater. Adv. Technol.*, vol. 186, no. 1, pp. 48–53, 2014, doi: 10.1016/j.mseb.2014.03.009.

[23] E. M. Masoud, A. A. El-Bellihi, W. A. Bayoumy, and M. A. Mousa, “Organic-inorganic composite polymer electrolyte based on PEO-LiClO 4 and nano-Al2O3 filler for lithium polymer batteries: Dielectric and transport properties,” *J. Alloys Compd.*, vol. 575, pp. 223–228, 2013, doi: 10.1016/j.jallcom.2013.04.054.

[24] M. Ravi, K. Kiran Kumar, V. Madhu Mohan, and V. V. R. Narasimha Rao, “Effect of nano TiO2 filler on the structural and electrical properties of PVP based polymer electrolyte films,” *Polym. Test.*, vol. 33, pp. 152–160, 2014, doi: 10.1016/j.polymertesting.2013.12.002.

[25] K. K. Wimalaweera, V. A. Seneviratne, and M. A. K. L. Dissanayake, “EFFECT OF Al 2 O 3 CERAMIC FILLER ON THERMAL AND TRANSPORT PROPERTIES OF POLY(ETHYLENE OXIDE)-LITHIUM PERCHLORATE SOLID POLYMER ELECTROLYTE,” *Procedia Eng.*, vol. 215, no. 2017, pp. 109–114, 2017, doi: 10.1016/j.proeng.2018.02.082.

[26] R. Zhang, M. Hummelgård, and H. Olin, “A facile one-step method for synthesising a parallelogram-shaped single-crystalline ZnO nanosheet,” *Mater. Sci. Eng. B Solid-State Mater. Adv. Technol.*, vol. 184, no. 1, pp. 1–6, 2014, doi: 10.1016/j.mseb.2013.12.009.

[27] S. A. Hashmi, M. Y. Bhat, M. K. Singh, N. T. K. Sundaram, B. P. C. Raghupathy, and H. Tanaka, “Ionic liquid-based sodium ion-conducting composite gel polymer electrolytes: effect of active and passive fillers,” *J. Solid State Electrochem.*, vol. 20, no. 10, pp. 2817–

2826, 2016, doi: 10.1007/s10008-016-3284-6.

[28] J. Sharma and S. Hashmi, "Magnesium ion-conducting gel polymer electrolyte nanocomposites: Effect of active and passive nanofillers," *Polym. Compos.*, vol. 40, no. 4, pp. 1295–1306, 2019, doi: 10.1002/pc.24853.

[29] J. Cui *et al.*, "Solid polymer electrolytes with flexible framework of SiO2 nanofibers for highly safe solid lithium batteries," *Polymers (Basel).*, vol. 12, no. 6, 2020, doi: 10.3390/POLYM12061324.

[30] S. Sen Chi, Y. Liu, N. Zhao, X. Guo, C. W. Nan, and L. Z. Fan, "Solid polymer electrolyte soft interface layer with 3D lithium anode for all-solid-state lithium batteries," *Energy Storage Mater.*, vol. 17, no. July 2018, pp. 309–316, 2019, doi: 10.1016/j.ensm.2018.07.004.

[31] J. Bae, Y. Li, F. Zhao, X. Zhou, Y. Ding, and G. Yu, "Designing 3D nanostructured garnet frameworks for enhancing ionic conductivity and flexibility in composite polymer electrolytes for lithium batteries," *Energy Storage Mater.*, vol. 15, no. March, pp. 46–52, 2018, doi: 10.1016/j.ensm.2018.03.016.

[32] S. Rajendran, M. Sivakumar, and R. Subadevi, "Effect of salt concentration in poly(vinyl alcohol)-based solid polymer electrolytes," *J. Power Sources*, vol. 124, no. 1, pp. 225–230, 2003, doi: 10.1016/S0378-7753(03)00591-3.

[33] Z. Zhang, Y. Huang, H. Gao, J. Hang, C. Li, and P. Liu, "MOF-derived ionic conductor enhancing polymer electrolytes with superior electrochemical performances for all solid lithium metal batteries," *J. Memb. Sci.*, vol. 598, no. December 2019, p. 117800, 2020, doi: 10.1016/j.memsci.2019.117800.

[34] M. Yao, T. Yu, Q. Ruan, Q. Chen, H. Zhang, and S. Zhang, "High-Voltage and Wide-Temperature Lithium Metal Batteries Enabled by Ultrathin MOF-Derived Solid Polymer Electrolytes with Modulated Ion Transport," *ACS Appl. Mater. Interfaces*, vol. 13, no. 39, pp. 47163–47173, 2021, doi: 10.1021/acsami.1c15038.

[35] P. Guo, M. Song, and Y. Wang, "Promising application of MOF as composite solid electrolytes via clathrates of ionic liquid," *Inorganica Chim. Acta*, vol. 491, no. January, pp. 128–131, 2019, doi: 10.1016/j.ica.2019.02.038.

[36] D. E. Mathew, S. Gopi, M. Kathiresan, A. M. Stephan, and S. Thomas, “Influence of MOF ligands on the electrochemical and interfacial properties of PEO-based electrolytes for all-solid- state lithium batteries,” *Electrochim. Acta*, vol. 319, pp. 189–200, 2019, doi: 10.1016/j.electacta.2019.06.157.

[37] S. K. Fullerton-Shirey and J. K. Maranas, “Effect of LiClO 4 on the structure and mobility of PEO-based solid polymer electrolytes,” *Macromolecules*, vol. 42, no. 6, pp. 2142–2156, 2009, doi: 10.1021/ma802502u.

[38] J. Mindemark, M. J. Lacey, T. Bowden, and D. Brandell, “Beyond PEO—Alternative host materials for Li+-conducting solid polymer electrolytes,” *Prog. Polym. Sci.*, vol. 81, pp. 114–143, 2018, doi: 10.1016/j.progpolymsci.2017.12.004.

[39] G. M. Wu, S. J. Lin, and C. C. Yang, “Preparation and characterization of PVA/PAA membranes for solid polymer electrolytes,” *J. Memb. Sci.*, vol. 275, no. 1–2, pp. 127–133, 2006, doi: 10.1016/j.memsci.2005.09.012.

[40] A. Manthiram, X. Yu, and S. Wang, “Lithium battery chemistries enabled by solid-state electrolytes,” *Nat. Rev. Mater.*, vol. 2, no. 4, pp. 1–16, 2017, doi: 10.1038/natrevmats.2016.103.

[41] L. Zhu, P. Zhu, Q. Fang, M. Jing, and X. Shen, “Electrochimica Acta A novel solid PEO / LLTO-nanowires polymer composite electrolyte for solid-state lithium-ion battery,” *Electrochim. Acta*, vol. 292, pp. 718–726, 2018, doi: 10.1016/j.electacta.2018.10.005.

[42] S. Y. Jung, R. Rajagopal, and K. S. Ryu, “Synthesis and electrochemical performance of (100−x)Li7P3S11-xLi2OHBr composite solid electrolyte for all-solid-state lithium batteries,” *J. Energy Chem.*, vol. 47, pp. 307–316, 2020, doi: 10.1016/j.jechem.2020.02.018.

[43] N. Bonanos, K. S. Knight, and B. Ellis, “Perovskite solid electrolytes: Structure, transport properties and fuel cell applications,” *Solid State Ionics*, vol. 79, no. C, pp. 161–170, 1995, doi: 10.1016/0167-2738(95)00056-C.

[44] B. Huang *et al.*, “Li-Ion Conduction and Stability of Perovskite Li3/8Sr7/16Hf1/4Ta3/4O3,” *ACS Appl. Mater. Interfaces*, vol. 8, no. 23, pp. 14552–14557, 2016, doi: 10.1021/acsami.6b03070.

[45] K. Kim and D. J. Siegel, “Multivalent Ion Transport in Anti-Perovskite Solid Electrolytes,” *Chem. Mater.*, vol. 33, no. 6, pp. 2187–2197, 2021, doi: 10.1021/acs.chemmater.1c00096.

[46] Y. Li *et al.*, “A Perovskite Electrolyte That Is Stable in Moist Air for Lithium-Ion Batteries,” *Angew. Chemie - Int. Ed.*, vol. 57, no. 28, pp. 8587–8591, 2018, doi: 10.1002/anie.201804114.

[47] K. Liu, M. Wu, L. Wei, Y. Lin, and T. Zhao, “A composite solid electrolyte with a framework of vertically aligned perovskite for all-solid-state Li-metal batteries,” *J. Memb. Sci.*, vol. 610, no. November 2019, p. 118265, 2020, doi: 10.1016/j.memsci.2020.118265.

[48] F. Z. T. Yang, V. K. Peterson, and S. Schmid, “Composition and temperature dependent structural investigation of the perovskite-type sodium-ion solid electrolyte series Na1/2−xLa1/2−xSr2xZrO3,” *J. Alloys Compd.*, vol. 863, p. 158500, 2021, doi: 10.1016/j.jallcom.2020.158500.

[49] H. H. Sumathipala, M. A. K. L. Dissanayake, and A. R. West, “Novel LISICON mixed conductors, $Li_{4-2x}Co_xGeO_4$,” *Solid State Ionics*, vol. 31, no. 86–88, pp. 719–724, 1996, doi: 10.1109/6.249069.

[50] B. Zhang, L. Yang, L. W. Wang, and F. Pan, “Cooperative transport enabling fast Li-ion diffusion in Thio-LISICON Li10SiP2S12 solid electrolyte,” *Nano Energy*, vol. 62, no. May, pp. 844–852, 2019, doi: 10.1016/j.nanoen.2019.05.085.

[51] L. Bi *et al.*, “Critical roles of RuO2 nano-particles in enhancing cyclic and rate performance of LISICON Li3V2(PO4)3 cathode materials,” *J. Alloys Compd.*, vol. 845, p. 156271, 2020, doi: 10.1016/j.jallcom.2020.156271.

[52] N. J. Dudney, “Addition of a thin-film inorganic solid electrolyte (Lipon) as a protective film in lithium batteries with a liquid electrolyte,” *J. Power Sources*, vol. 89, no. 2, pp. 176–179, 2000, doi: 10.1016/S0378-7753(00)00427-4.

[53] Y. Hamon *et al.*, “Influence of sputtering conditions on ionic conductivity of LiPON thin films,” *Solid State Ionics*, vol. 177, no. 3–4, pp. 257–261, 2006, doi: 10.1016/j.ssi.2005.10.021.

[54] K. Senevirathne, C. S. Day, M. D. Gross, A. Lachgar, and N. A. W. Holzwarth, “A new

crystalline LiPON electrolyte: Synthesis, properties, and electronic structure," *Solid State Ionics*, vol. 233, pp. 95–101, 2013, doi: 10.1016/j.ssi.2012.12.013.

[55] A. S. Westover, N. J. Dudney, R. L. Sacci, and S. Kalnaus, "Deposition and Confinement of Li Metal along an Artificial Lipon-Lipon Interface," *ACS Energy Lett.*, vol. 4, no. 3, pp. 651–655, 2019, doi: 10.1021/acsenergylett.8b02542.

[56] W. C. West, J. F. Whitacre, and J. R. Lim, "Chemical stability enhancement of lithium conducting solid electrolyte plates using sputtered LiPON thin films," *J. Power Sources*, vol. 126, no. 1–2, pp. 134–138, 2004, doi: 10.1016/j.jpowsour.2003.08.030.

[57] T. Takahashi, K. Kuwabara, and M. Shibata, "Solid-state ionics - conductivities of Na+ ion conductors based on NASICON," *Solid State Ionics*, vol. 1, no. 3–4, pp. 163–175, 1980, doi: 10.1016/0167-2738(80)90001-6.

[58] S. Naqash, Q. Ma, F. Tietz, and O. Guillon, "Na3Zr2(SiO4)2(PO4) prepared by a solution-assisted solid state reaction," *Solid State Ionics*, vol. 302, pp. 83–91, 2017, doi: 10.1016/j.ssi.2016.11.004.

[59] B. Yan *et al.*, "NASICON-structured solid-state electrolyte Li 1.5 Al 0.5-x Ga x Ge 1.5 (PO 4) 3 prepared by microwave sintering," *Mater. Technol.*, vol. 34, no. 6, pp. 356–360, 2019, doi: 10.1080/10667857.2018.1563964.

[60] M. Monchak *et al.*, "Lithium Diffusion Pathway in Li1.3Al0.3Ti1.7(PO4)3 (LATP) Superionic Conductor," *Inorg. Chem.*, vol. 55, no. 6, pp. 2941–2945, 2016, doi: 10.1021/acs.inorgchem.5b02821.

[61] V. Epp, Q. Ma, E. M. Hammer, F. Tietz, and M. Wilkening, "Very fast bulk Li ion diffusivity in crystalline Li1.5Al0.5Ti1.5(PO4)3 as seen using NMR relaxometry," *Phys. Chem. Chem. Phys.*, vol. 17, no. 48, pp. 32115–32121, 2015, doi: 10.1039/c5cp05337d.

[62] Z. Kou, C. Miao, Z. Wang, and W. Xiao, "Novel NASICON-type structural Li1.3Al0.3Ti1.7SixP5(3-0.8x)O12 solid electrolytes with improved ionic conductivity for lithium ion batteries," *Solid State Ionics*, vol. 343, no. August, p. 115090, 2019, doi: 10.1016/j.ssi.2019.115090.

[63] M. Weiss, D. A. Weber, A. Senyshyn, J. Janek, and W. G. Zeier, "Correlating Transport and Structural Properties in Li1+ xAlxGe2- x(PO4)3 (LAGP) Prepared from Aqueous

Solution," *ACS Appl. Mater. Interfaces*, vol. 10, no. 13, pp. 10935–10944, 2018, doi: 10.1021/acsami.8b00842.

[64] Q. Liu *et al.*, "Self-Healing Janus Interfaces for High-Performance LAGP-Based Lithium Metal Batteries," *ACS Energy Lett.*, vol. 5, no. 5, pp. 1456–1464, 2020, doi: 10.1021/acsenergylett.0c00542.

[65] Q. Liu *et al.*, "Safe LAGP-based all solid-state Li metal batteries with plastic super-conductive interlayer enabled by in-situ solidification," *Energy Storage Mater.*, vol. 25, no. September 2019, pp. 613–620, 2020, doi: 10.1016/j.ensm.2019.09.023.

[66] Q. Guo *et al.*, "New Class of LAGP-Based Solid Polymer Composite Electrolyte for Efficient and Safe Solid-State Lithium Batteries," *ACS Appl. Mater. Interfaces*, vol. 9, no. 48, pp. 41837–41844, 2017, doi: 10.1021/acsami.7b12092.

Chapter: 3 Review on Experimentation and Characterization Methods

3.1 Synthesis Method

For the proper synthesis of the electrolyte material in the lab, many methods have been devised. Among them, some methods require special equipment while others can be performed without them. Choice of the synthesis process to form mainly rests on the preferred size, suitable properties of the surface, and the kind of material that is concerned such as semiconductors, metals, polymers, ceramics, etc. These methods have been researched and improved to increase the yield of SSEs, obtain better structural properties and purity. Some of these methods have been discussed below:

3.1.1 Solid-state method

Solid state method has a simple fabrication process, is characterized by large scale production and low cost at room temperature and ambient pressure. The size can also be reduced, and uniform nanomaterials can be synthesized in massive amounts in short time. During SSEs fabrication finely ground powders can be obtained, these powders not only have good interfacial contact but also contain homogeneity in phases and low sintering temperatures. It was observed through experimentation that the grain resistance of LTP samples did not change by this synthesis method, however the activation energy decreased, and the grain boundary resistance was altered[1]. The fabrication of LTP by mechanical activation method assisted by lithium fluoride LiF produced dense electrolytes with sharp crystal peaks and high conductivity of 2.318×10^{-4} S/cm. similarly without pre assisted the formation of LATP sintered at 900 ℃ for 6 h also produced excellent electrochemical performance. The main disadvantage of this method if=s the formation of cracks, pores and voids which block the pathways at grain boundaries resulting in poor performance of the SSE.

The steps involved in solid-state method include:

1. Appropriate material selection
2. Mixing of materials
3. Pellets formation

4. Thermal treatment
5. Analysis

3.1.1.1 Appropriate material selection

The materials selected are usually fine powders in powders to maximize the surface area for contact between particles. These materials should be highly reactive and not inert. The composition should be well defined in start. For LATP SSE the starting materials are usually lithium carbonate Li_2CO_3, aluminum oxide Al_2O_3, titanium oxide TiO_2, and ammonium dihydrogen phosphate $NH_2H_2PO_4$[2].

3.1.1.2 Mixing

The fine ground materials are thoroughly mixed by mortar and pestle for 15-20 minutes. However, in case of oxide the planetary ball milling is used to for mixing.

3.1.1.3 Calcination

In order to decompose certain products, form the staring material and obtain the desired product the starting materials are given a heat treatment. In case of LATP the volatile products are carbon dioxide CO_2, water H_2O and ammonia NH_3 and the $NH_2H_2PO_4$ is decomposed to give a phosphate ion PO_4^-.

3.1.1.4 Pellets formation

To increase the contact between the reagents and decrease the contact with the sample crucible the pellets are formed at a certain pressure. An organic binder is sometimes used to hold the material together in pellet form [3].

3.1.1.5 Thermal treatment

For the reaction of oxide and formation desired product the sample is sintered at a certain temperature. The factors affecting the temperature choice include Tamman’s rule and volatilization potential. According to Tamman’s rule the reaction does not occur until the temperature reaches the 2/3 of melting point of one of reagents. The atmosphere of reaction is also very critical to the reaction.

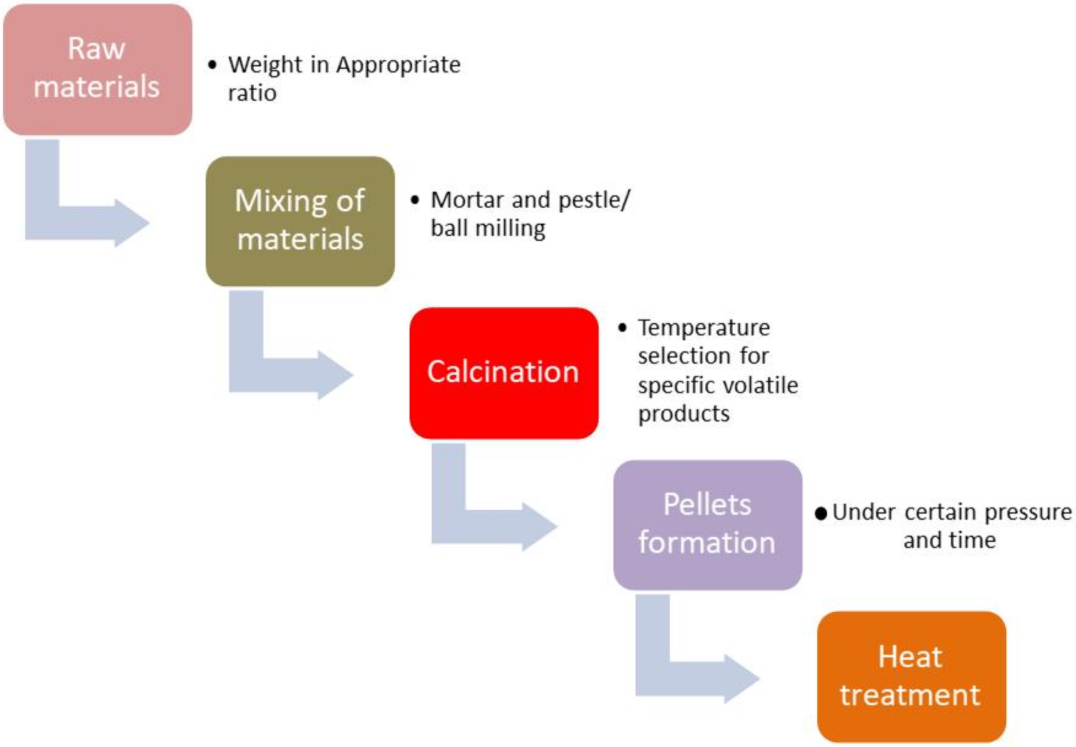

Figure 3.1: Flow chart of solid-state synthesis method

3.1.2 Sol-gel synthesis

Sol-gel synthesis method produces high crystalline nanoparticles, homogeneous phases, reduced particle size, well defined morphology, uniform distribution of particles and accurate molar ratio. The sintering temperature is very less, and this process consumes less energy as compared to solid-state method. Sol stands for solution, in this process a sol is formed by hydrolysis reaction, the solution is left to form polymer chains and condense to form the gel like substrate. The gel formation occurs at certain temperature and heat treatment[4].

Wu et al. synthesized the LATP electrolyte by sol-gel method using organic compounds, the conductivity obtained was 1.2×10^{-4} S/cm which is higher than solid-state reaction prepared LATP. The extensive and sensitive method of gel formation limits its use in large scale production of ASSLBs[5]. The phosphate ion was not soluble in alcohol solutions therefor, Schroeder et al. synthesized the LATP electrolyte by using water and ethanol as solvents for gel formation and addition of nitric acid helped in the solubility of phosphate group. The detail synthesis procedure by sol-gel method is discussed in figure below.

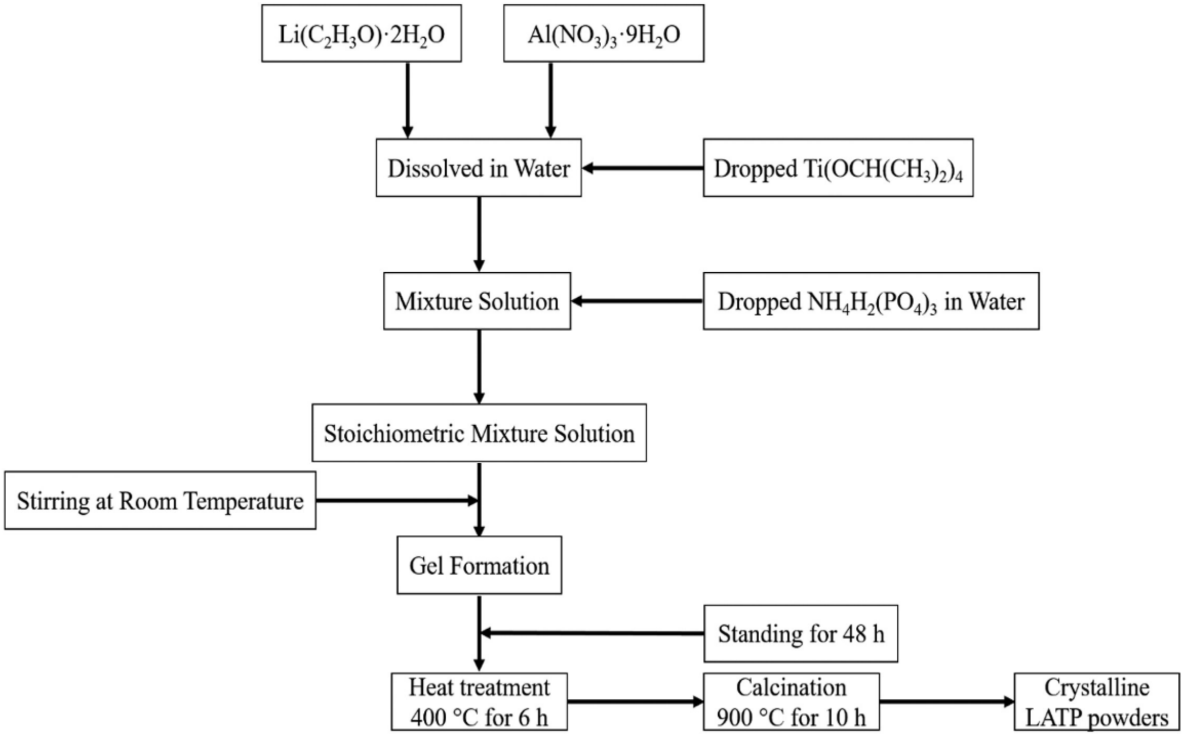

Figure 3.2: Sol-gel method for synthesis of LATP SSE

3.1.3 Solvothermal Synthesis

It is a technique used for making a range of materials like semiconductors, metals, polymers, and ceramics. The method involves a solvent at moderate to high pressure (typically between 1atm and 10,000 atm) and temperature (from 100 °C to 1000°C) which helps precursors in interaction during synthesis. If the solvent used is water, then the process is known as the "hydrothermal process." The conditions of the hydrothermal synthesis process are usually kept at the supercritical temperature of water (374 °C)[6]. This method can be performed to make a wide variety of geometries such as thin films, single crystals, bulk powders, and nanocrystals. In addition, the formation (rod (2D), sphere (3D), and wire (1D) of crystals are organized by the control of chemical of interest concentration, solvent supersaturation, and control on kinetic. It can be used to form stagnant and thermodynamically stable forms involving novel elements that are not easily constructed from other synthetic paths. This review will emphasize some recent advances including the solvothermal process and nanocrystalline because in the last decade 80% of the literature focused on nanocrystals[7].

3.1.4 Hydrothermal Synthesis

This method is used to synthesize materials that require special conditions for the synthesis. Also, this method helps control the structure, morphology, and other properties of the material. Metal oxides, halides, composites that require specific temperature as well as pressure are usually synthesized by this method[8]. The nanoparticles obtained by this method have characteristic properties. This method normally requires the use of an autoclave device in which temperature and pressure can be simultaneously controlled. The main significance of this process is the ability to synthesize a wide number of NPs that have upgraded composition, size, structure, and chemistry of surface that is reasonably cheap[9].

3.1.5 Pyrolysis

During pyrolysis, organic matter is decomposed into no condensable gases, condensable liquids, and biochar or charcoal as a residual solid product in an inert environment without oxygen.

3.2 Characterization Techniques

3.2.1 X-Ray Diffraction (XRD)

This is one of the most important and common material characterization technique which provides information about the morphology, components, and crystallite size of the material. It uses X-ray radiations that pass through the material at an angle to the source. The diffraction angle is calculated, and the intensity is recorded. At an angle how many radiations deflect from a specific plane on the material gives information regarding its structure morphology[10].

To find evidence about the configuration of X-ray diffraction (XRD) of crystalline materials depend on the double particle/wave nature of X-rays. Identification and characterization of materials centered on their X-ray form are the major uses of the procedure[11]. When a monochromatic X-rays incident beam contacts an object material the first outcome that takes place is atoms within the target substance scatter those X-rays as shown in Figure 3.3. The spread X-rays undertake destructive and constructive interference in the substances having proper structure (i.e. crystalline), which is called diffraction. The X-rays diffraction by crystals is described by Bragg‟s Law,

$$\mathrm{n}(\lambda) = 2\mathrm{d}\,\mathrm{Sin}(\theta) \tag{1}$$

The shape and size of the materials unit cell determine directions of likely diffractions[12]. The atom's arrangement in the crystal structure affects the diffracted wave intensities. Many materials are not one crystal rather are comprised of little, small crystallites in all likely directions which are called polycrystalline powder or aggregate. When a material with casually focused crystallites is put in an X-ray, the beam will view all available interatomic planes. If the experimental angle is scientifically altered, then all the available diffraction peaks from the substance will be identified [13].

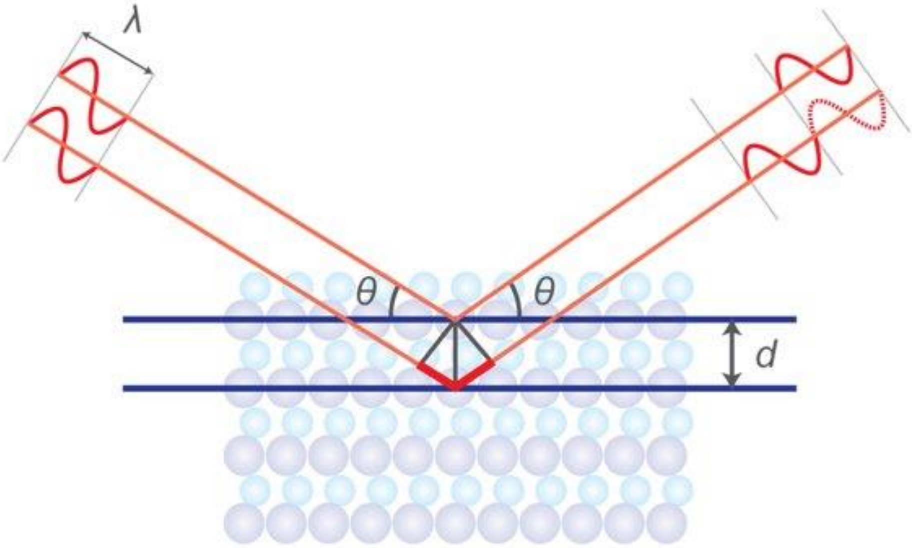

Figure 3.3: The Bragg's Law

3.2.2 Scanning Electron Microscopy

SEM utilizes a high-energy electrons-focused ray to produce a wide range of signals at the solid surface of the specimen. The high-energy electrons penetrate through the material and escape through the other end as shown in Figure 3.4. The information of the substance like chemical composition, crystalline structure, external morphology (texture), and materials orientation will be revealed signals of the electron beam and sample interactions. In various applications, a 2-dimensional image is created that shows spatial variations in these properties, and numbers are collected over a particular choice area of the sample surface[14]. The scanning method by simple SEM practices (magnification varying from 20X to around 30,000X, 3-D resolution of 50 to 100 nm) can be used to distinguish the areas that vary in size from about 1 cm to 5 microns in breadth. This method is exclusively valuable in semi quantitatively or qualitatively identifying chemical contents (by EDS), crystal orientations (using EBSD), and crystalline structure. The SEM is proficient in executing analyses of a specific area or point locations on the sample object.

Its design and function are quite comparable to the EPMA and significant connections in abilities remain between the two devices[15].

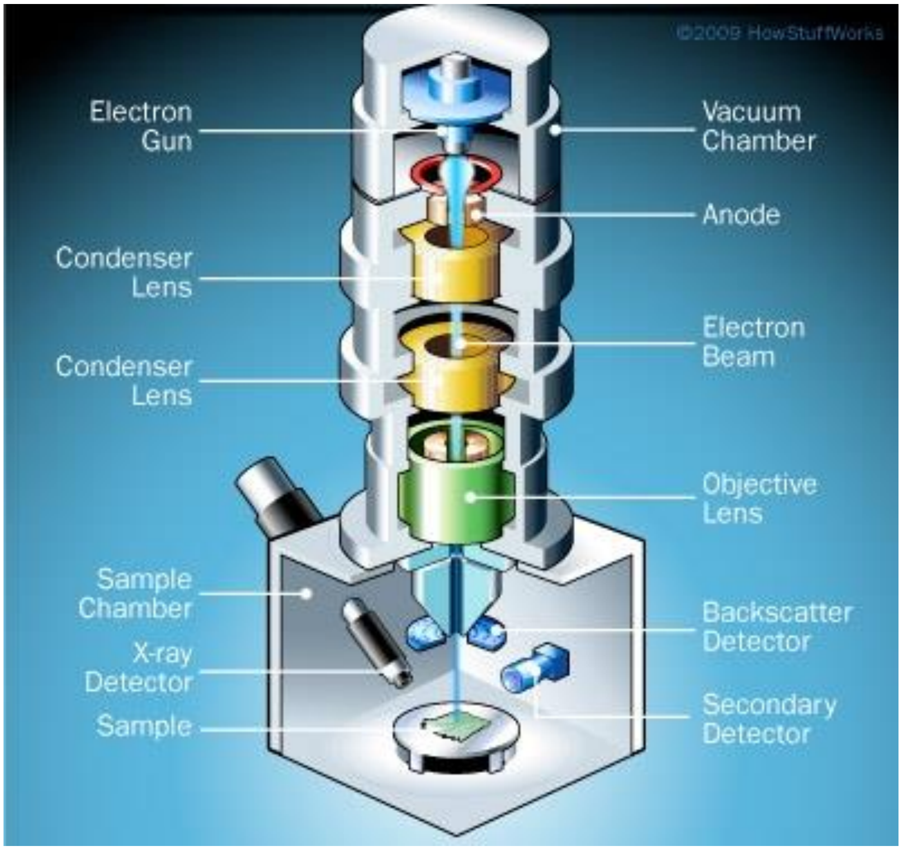

Figure 3.4: Illustration of how SEM works

3.2.3 Energy Dispersive X-ray Spectroscopy (EDX)

EDS is an elemental analysis method used to quantify the number of individual elements present in a nanoparticle. This technique gives the number of substances at a particular point but does not give the overall quantity of each element. It is usually combined with SEM or TEM to get a nanoscale image of particles through them, and EDS performs the analysis of that nanostructure. In the early 1970s, EDS developed into one commercial product and rapidly crossed WDS in popularity[16]. The overall structure of the EDS is very simple because of no moving parts like the rotation detector in WDS. The sensor gathers the X-rays energies signal from all series elements in a sample at a similar time as compared to gathering signals from X-ray wavelength one by one which makes the EDS systems relatively fast as seen in Figure 3.5. The characteristic energy dispersion resolution is around 150–200 eV, which is lower than WDS resolve. The lightest component that can be identified is not C (Z=6) rather O (Z=8). But major benefits like low cost and fast analysis make these disadvantages insignificant.

EDS band is a graph between the power of X-rays and the corresponding energies. Both light and heavy elements can be seen in a range of spectrum from 0.1 to 10-20 keV because both M or L lines of heavy elements and K lines of light elements are evident in this array[17].

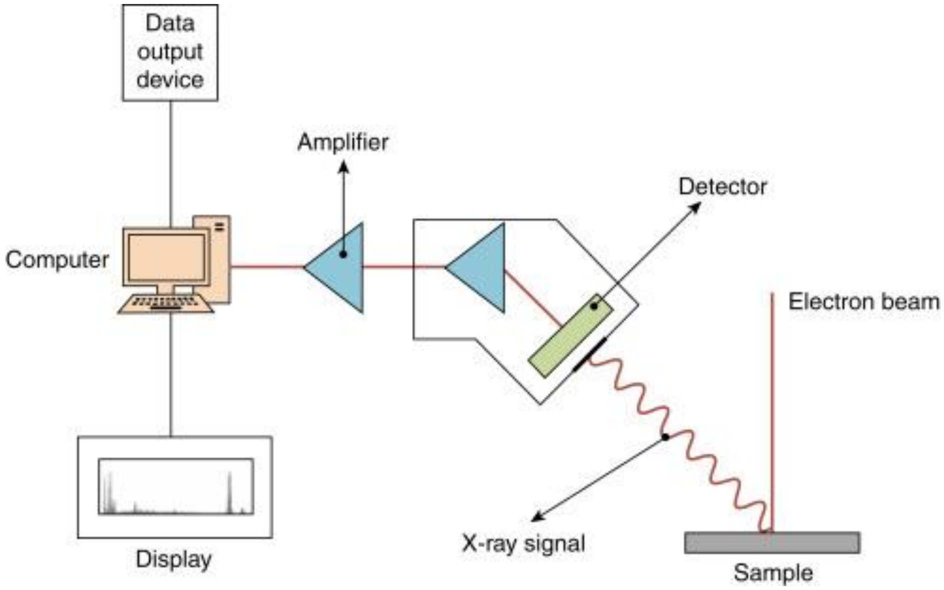

Figure 3.5: Illustration of EDX

3.2.4 Fourier Transform Infrared Spectroscopy

Fourier transform infrared spectroscopy is the preferred technique for infrared spectroscopy. When IR radiation passes through a material, some of the incident radiation gets absorbed in the material while the rest is transmitted Figure 3.6. The detector at the other end detects the transmitted radiation and sets out a signal that is basically represented in the form of a spectrum and it demonstrates the molecular nature of the material[19].

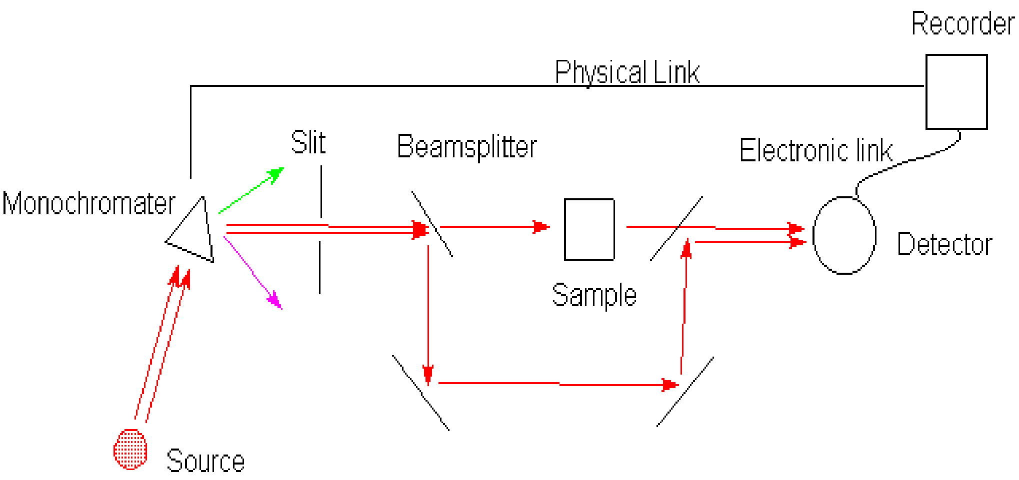

Figure 3.6: Schematic diagram of FTIR

3.2.5 Xray Photoelectron Spectroscopy (XPS)

XPS technique is used for the identification of elements within a material, oxidation state, electronic structure, and density of material. The elements on the surface in case of thin films fabrication can also be determined by this technique. XPS is a strong measuring technique since it displays not only the details of elements, but also to what other elements they are linked. The depth profiling and line profiling elemental composition can also be studied in detail be combining it with ion-beam etching [21]. To measure the chemical states of elements the quantity and kinetic energy of electrons is used. High vacuum ~106 Pa or ultra-high vacuum ~107 Pa are required for XPS, while ambient pressures(~ten millibars), is used [22].

Because it produces good quantitative precision from homogenous solid-state materials, XPS is often used to construct empirical formulas. Absolute quantification necessitates the use of certified samples as reference, this type of quantification is more difficult less prevalent. Under ideal conditions, the atomic percent (at percent) values computed from the primary XPS peaks have a quantitative accuracy of 90-95 percent for each peak. For correct reporting of quantitative data, quantitative accuracy is critical [23].

3.3 Electrochemical Techniques

3.3.1 Electrochemical Impedance Spectroscopy (EIS)

This technique of electrochemical workstation allows us to measure the resistivity of our system. This includes resistance of electrolyte, ohmic loss and or activation losses. Electrical resistance is the measure of the of a circuit element that resists current flow.

$$R = E/I \qquad (2)$$

According to Ohm's law, R is the resistance which is defined as the ratio of voltage (E), and current (I)[24]. This known law use is limited to only one circuit element, the ideal resistor.
An ideal resistor has several simplifying properties:

- Ohm's Law is followed at every range of current and voltage.
- Resistance is not dependent on the frequency.
- The voltage passing through a resistor and the AC current are in a single phase.

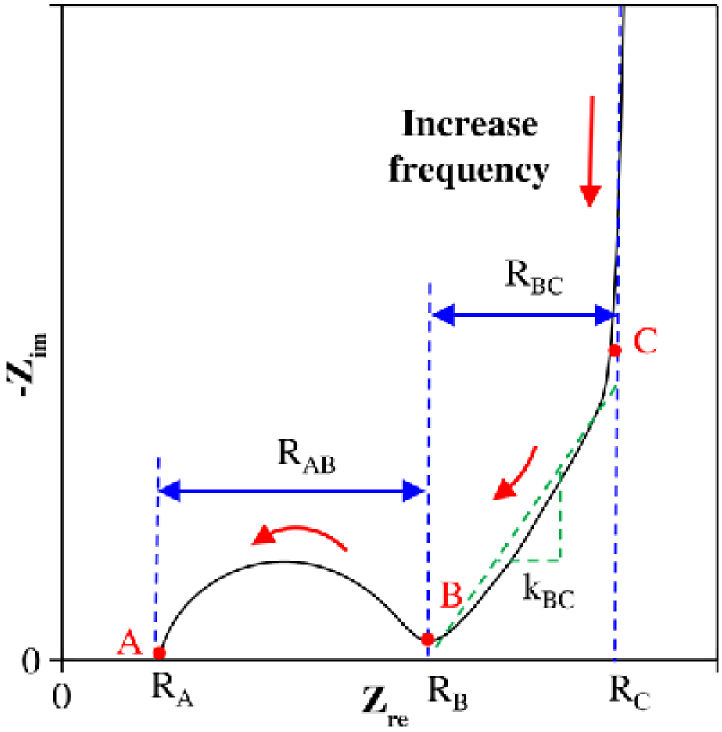

Figure 3.7: EIS Profile (Nyquist Plot)

Summary

This chapter initially discusses different chemical synthesis methods like solvothermal and hydrothermal method. After that material characterization techniques have been studied i.e., XRD, SEM, EDS, TGA, BET, NEXAF and FTIR. Main principle of these techniques has been noted down along with diagrams. After that the whole electrochemical testing process implemented was explained including ink formation, ink deposition on substrate and electrochemical performance determination using various techniques like CV, CP, and EIS with a three-electrode system.

List of References

[1] T. Takahashi, K. Kuwabara, and M. Shibata, “Solid-state ionics - conductivities of Na+ ion conductors based on NASICON,” *Solid State Ionics*, vol. 1, no. 3–4, pp. 163–175, 1980, doi: 10.1016/0167-2738(80)90001-6.

[2] H. Rusdi, N. S. Mohamed, R. H. Y. Subban, and R. Rusdi, “Enhancement of electrical properties of NASICON-type solid electrolytes (LiSn2P3O12) via aluminium substitution,” *J. Sci. Adv. Mater. Devices*, vol. 5, no. 3, pp. 368–377, 2020, doi: 10.1016/j.jsamd.2020.06.003.

[3] F. Zheng, M. Kotobuki, S. Song, M. O. Lai, and L. Lu, “Review on solid electrolytes for all-solid-state lithium-ion batteries,” *J. Power Sources*, vol. 389, no. April, pp. 198–213, 2018, doi: 10.1016/j.jpowsour.2018.04.022.

[4] C.J. Brinker; G. W. Scherer, “Sol-Gel_Science_The_physics_and_chemistry_of_sol-gel_processing_-_Brinker_1990.pdf.” p. 462, 1990. doi: 10.1016/S0254-0584(02)00315-2.

[5] S. D. Lee *et al.*, “Composite Electrolyte for All-Solid-State Lithium Batteries: Low-Temperature Fabrication and Conductivity Enhancement,” *ChemSusChem*, vol. 10, no. 10, pp. 2175–2181, 2017, doi: 10.1002/cssc.201700104.

[6] J. Lai, W. Niu, R. Luque, and G. Xu, “Solvothermal synthesis of metal nanocrystals and their applications,” *Nano Today*, vol. 10, no. 2, pp. 240–267, 2015, doi: 10.1016/j.nantod.2015.03.001.

[7] X. Dong, M. Qi, Y. Tong, and F. Ye, “Solvothermal synthesis of single-crystalline hexagonal cobalt nanofibers with high coercivity,” *Mater. Lett.*, vol. 128, pp. 39–41, 2014, doi: 10.1016/j.matlet.2014.04.133.

[8] S. Sōmiya and R. Roy, “Hydrothermal synthesis of fine oxide powders,” *Bull. Mater. Sci.*, vol. 23, no. 6, pp. 453–460, 2000, doi: 10.1007/BF02903883.

[9] S. Feng and R. Xu, “New materials in hydrothermal synthesis,” *Acc. Chem. Res.*, vol. 34, no. 3, pp. 239–247, 2001, doi: 10.1021/ar0000105.

[10] H. Khan, A. S. Yerramilli, A. D’Oliveira, T. L. Alford, D. C. Boffito, and G. S. Patience,

"Experimental methods in chemical engineering: X-ray diffraction spectroscopy—XRD," *Can. J. Chem. Eng.*, vol. 98, no. 6, pp. 1255–1266, 2020, doi: 10.1002/cjce.23747.

[11] M. Y. A. Mollah, F. Lu, and D. L. Cocke, "An X-ray diffraction (XRD) and Fourier transform infrared spectroscopic (FT-IR) characterization of the speciation of arsenic (V) in Portland cement type-V," *Sci. Total Environ.*, vol. 224, no. 1–3, pp. 57–68, 1998, doi: 10.1016/S0048-9697(98)00318-0.

[12] J. Kacher, C. Landon, B. L. Adams, and D. Fullwood, "Bragg's Law diffraction simulations for electron backscatter diffraction analysis," *Ultramicroscopy*, vol. 109, no. 9, pp. 1148–1156, 2009, doi: 10.1016/j.ultramic.2009.04.007.

[13] Y. Leng, *Materials characterization: Introduction to microscopic and spectroscopic methods: Second edition*. 2013. doi: 10.1002/9783527670772.

[14] W. Zhou, R. Apkarian, Z. L. Wang, and D. Joy, "Fundamentals of scanning electron microscopy (SEM)," *Scanning Microsc. Nanotechnol. Tech. Appl.*, pp. 1–40, 2007, doi: 10.1007/978-0-387-39620-0_1.

[15] K. D. Parry V, "Microscopy : An introduction," *III-Vs Rev.*, vol. 13, no. 4, pp. 40–44, 2000.

[16] L. J. Allen, A. J. D'Alfonso, B. Freitag, and D. O. Klenov, "Chemical mapping at atomic resolution using energy-dispersive X-ray spectroscopy," *MRS Bull.*, vol. 37, no. 1, pp. 47–52, 2012, doi: 10.1557/mrs.2011.331.

[17] D. E. Newbury and N. W. M. Ritchie, "Is scanning electron microscopy/energy dispersive X-ray spectrometry (SEM/EDS) quantitative?," *Scanning*, vol. 35, no. 3, pp. 141–168, 2013, doi: 10.1002/sca.21041.

[18] T. C. Lovejoy *et al.*, "Single atom identification by energy dispersive x-ray spectroscopy," *Appl. Phys. Lett.*, vol. 100, no. 15, 2012, doi: 10.1063/1.3701598.

[19] B. A. Boukamp, "Fourier transform distribution function of relaxation times; application and limitations," *Electrochim. Acta*, vol. 154, pp. 35–46, 2015, doi: 10.1016/j.electacta.2014.12.059.

[20] C. Berthomieu and R. Hienerwadel, "Fourier transform infrared (FTIR) spectroscopy,"

Photosynth. Res., vol. 101, no. 2–3, pp. 157–170, 2009, doi: 10.1007/s11120-009-9439-x.

[21] J. M. Hollander, W. L. Jolly, and J. M. Hollander, “X-Ray Photoelectron Spectroscopy,” vol. 17, no. June, pp. 193–200, 1970.

[22] C. S. Fadley, “X-ray photoelectron spectroscopy: Progress and perspectives,” *J. Electron Spectros. Relat. Phenomena*, vol. 178–179, no. C, pp. 2–32, 2010, doi: 10.1016/j.elspec.2010.01.006.

[23] A. Proctor and P. M. A. Sherwood, “Data Analysis Techniques in X-ray Photoelectron Spectroscopy,” *Anal. Chem.*, vol. 54, no. 1, pp. 13–19, 1982, doi: 10.1021/ac00238a008.

[24] D. D. MacDonald, “Reflections on the history of electrochemical impedance spectroscopy,” *Electrochim. Acta*, vol. 51, no. 8–9, pp. 1376–1388, 2006, doi: 10.1016/j.electacta.2005.02.107.

[25] B. A. Mei, O. Munteshari, J. Lau, B. Dunn, and L. Pilon, “Physical Interpretations of Nyquist Plots for EDLC Electrodes and Devices,” *J. Phys. Chem. C*, vol. 122, no. 1, pp. 194–206, 2018, doi: 10.1021/acs.jpcc.7b10582.

[26] J. Huang, Z. Li, B. Y. Liaw, and J. Zhang, “Graphical analysis of electrochemical impedance spectroscopy data in Bode and Nyquist representations,” *J. Power Sources*, vol. 309, pp. 82–98, 2016, doi: 10.1016/j.jpowsour.2016.01.073.

Chapter: 4 Methodology and Experimentation

4.1 Chemical Reagents

All the chemical reagents were purchased from Sigma Aldrich with analytical purity. The common materials for LATP, LAYTP and LAYTSP are lithium nitrate, aluminum nitrate nanohydrate, titanium oxide and ammonium dihydrogen phosphate. The dopants used were yttrium nitrate hexahydrate and silicon dioxide.

4.2 Material Synthesis

4.2.1 Synthesis of LAYTSP

The pellets of $Li_{1.7}Al_{0.225}Y_{0.075}Ti_{1.7}Si_{0.4}P_{2.6}O_{12}$ (LAYTSP) solid electrolyte were prepared by adding 4.4571g of $LiNO_3$, 1.8390g of Al $(NO_3)_3.9H_2O$, 1.1023g of Y $(NO_3)_3$ $.6H_2O$, 0.9153g of SiO_2, 5.2100g of TiO_2, and 11.4762g of $NH_4H_2PO_4$ with total material weight of 25g. The powders were ground and mixed in agate mortar and pestle for 15 minutes. The mixture was transferred to ZrO_2 jars containing 10 ZrO_2 balls with a weight ratio of 1:20 and mechanically activated by planetary ball milling apparatus (High-Speed Shimmy Ball Mill SFM-1 (QM-3SP2)) at 500 rpm for 6 hours with intervals to avoid heating of the apparatus. The mixture was calcined in an alumina boat at 500 °C for 4 hours at a heating rate of 10 °C/min under constant air in a box resistance furnace (model: SX-2.5-10). After cooling to room temperature, the mixture was ground to a fine powder in pestle and mortar for 10 minutes. In the next step, pellets were made under the pressure of 10MPa for 30 minutes and with a diameter of 10mm each. These pellets were sintered at different temperature ranges i.e., 800 °C, 850 °C, and 900 °C for 5 hours respectively under constant air with a heating rate of 10 °C/min in box furnace. Below 800 °C the sample showed no weight loss hence the reaction didn’t occur[1]. Each pellet was naturally cooled and collected in an airtight glass sample vial 15ml.

4.2.2 Synthesis of LATP and LAYTP:

The undoped LATP pellet was prepared by adding 2.4061 g of $LiNO_3$, 1.2439 g of Al $(NO_3)_3.9H_2O$, 2.6431 g of TiO_2, and 8.707 g of $NH_4H_2PO_4$ with total material weight 15 g.

similarly, for LAYTP the total weight of powders was also 15 g with 2.3917 g of $LiNO_3$, 0.9273 g of $Al(NO_3)_3.9H_2O$, 0.3990 g of $Y(NO_3)_3.6H_2O$, 2.6272 g of TiO_2, and 8.6548 g of $NH_4H_2PO_4$. The same step by step method was followed for the synthesis of both LATP and LAYTP, the sintering was done at only 900 °C.

4.3 Material Characterization

4.3.1 Xray Diffraction (XRD)

The phase assembly and sample purity were examined using a Bruker D8 Advance diffractometer with LYNXEYE detector and Cu-kα radiation. The data was taken in range of 10°–80° with 0.02° per step.

4.3.2 Scanning Electron Microscopy (SEM)

VEGA3, 51–ADD0007 (Tescan, Brno, Czech Republic) SEM was used to study the morphology of the samples.

4.3.3 Fourier-transform Infrared Spectroscopy (FTIR)

FTIR spectra of the samples were collected in the range of 600-4000 cm^{-1} using a Cary 630 FTIR spectrometer.

4.3.4 X-ray photoelectron spectroscopy (XPS)

The composition and chemical states of elements in each sample are studied using model PHI 5000 VersaProbe (Ulvac-PHI, Japan) with monochromatic Al-Kα source.

4.3.5 Electrochemical Impedance Spectroscopy (EIS)

Gold (Au) layer was deposited on both sides of the pellet before ac impedance measurements. Vacuum spin coater was used for deposition and each side of the pellet was kept in the spinner for about 15 minutes[2]. This gold layer acts as ion-blocking electrodes. AC impedance measurements were taken by CHI660E (Shanghai Chenhua Co., Ltd.) potentiostat at a scan frequency of 0.001–1MHz with an amplitude of 10 mV. The ionic conductivity is calculated using equation, in which σ, t, d, and R denote the ionic conductivity, thickness, diameter of the pellets and total resistance [3]. The total resistance is the sum of both grain resistance and grain boundary resistance.

$$\sigma = \frac{4t}{\pi d^2 R} \qquad (3)$$

Summary

This chapter includes the total experimental procedure that was involved in the research process. The synthesis process of LATP, LAYTP and LAYTSP and their characterization techniques used were thoroughly demonstrated in the chapter. Finally, the electrochemical testing techniques which were used on electrochemical workstation and the testing parameters are discussed.

List of References

[1] E. Zhao *et al.*, “High ionic conductivity Y doped Li1.3Al0.3Ti1.7(PO4)3 solid electrolyte,” *J. Alloys Compd.*, vol. 782, pp. 384–391, 2019, doi: 10.1016/j.jallcom.2018.12.183.

[2] S. Breuer *et al.*, “Separating bulk from grain boundary Li ion conductivity in the sol-gel prepared solid electrolyte Li1.5Al0.5Ti1.5(PO4)3,” *J. Mater. Chem. A*, vol. 3, no. 42, pp. 21343–21350, 2015, doi: 10.1039/c5ta06379e.

[3] “Structure and ion transport of lithium-rich Li1+xAlxTi2−x(PO4)3 with A combined computational and experimental study.pdf.”

Chapter: 5 Results and Discussion

5.1 Material Characterization

5.1.1 Structural Analysis

Figure 5.1 shows the XRD patterns of LAYTSP particles at temperatures of 700°- 950° C. The diffraction peaks at 20.8° and 24.5° become sharper when the sintering temperature rises from 800 to 900 °C. The $LiTi_2(PO_4)_3$ phase with NASICON type structure is well assigned with (JCPDS#35-0754) [1], revealing that the pure phase NASICON-type Li1.3Al0.3Ti1.7(PO4)3 is successfully manufactured by solid-state method and at all sintering temperatures. The LATP has a low crystallinity at sintering temperatures of 800 °C and 850 °C than 900 °C where the sharpness of peak and peak intensity is greater. The impurity phase AlPO4 (JCPDS#48-0625) can be seen in figure, which results from the loss of lithium during the high sintering temperature and has a negative effect on grain boundary conductivity [2]. This impurity phase increase with increase in sintering temperature and blocks the lithium ion conducting pathways. Another phase $Li_4P_2O_7$ (JCPDS#77-1045) can also be detected around 26.8^0 this phase appears in the last sample since the lithium is oxidized [3]. Table 5.1 represents the lattice parameters and volume of LAYTSP samples. It is observed that with increase in temperature the lattice parameters increase in size thus volume increases indicating that Y^{+3} and Si^{+4} enter the lattice, the volume of unit cell of LAYTSP is greater than the base material LATP.

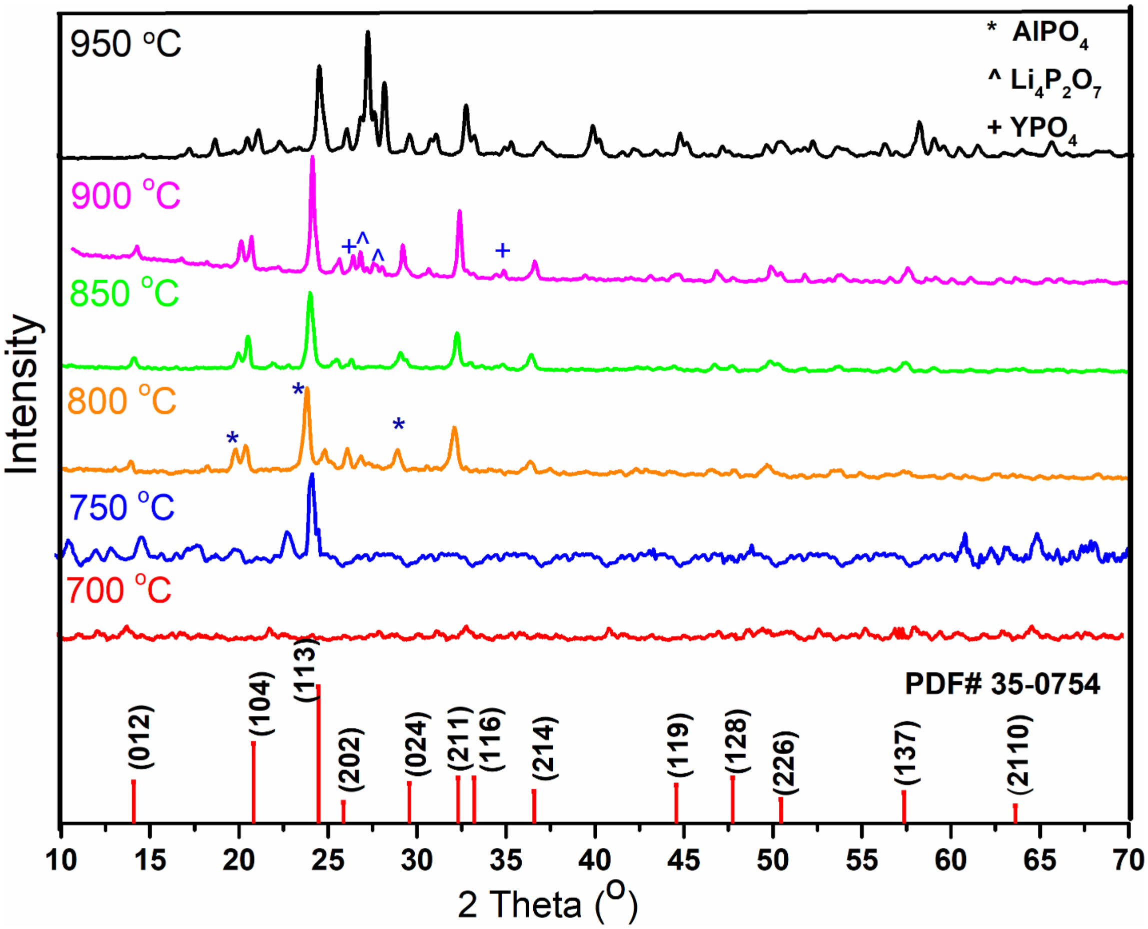

Figure 5.1: Xray diffraction of LAYTSP at different sintering temperatures 700 °C- 950 °C

Table 5.1: Lattice parameters of LAYTSP at different sintering temperatures.

Sintering Temperature	**Lattice parameters (Å)**			**volume**
°C	a	b	c	$Å^3$
800	8.3827	8.387	21.6265	1316.108
850	8.4349	8.4349	21.3925	1319.5309
900	8.4094	8.409	21.807	1335.569

Figure 5.2 represents the xrd patterns of LATP and LAYTP, every peak is well assigned with the (PDF# 35-0754) confirming that Nasicon phase $LiTi_2(PO_4)_3$ is successfully synthesized. It can be observed from the xrd patterns that the intensity of $AlPO_4$ decreases by adding a dopant in the lattice structure with yttrium and silicon co-doping some of $AlPO_4$ peaks are diminished. YPO_4

impurity can be observed in LAYTP and LAYTSP pattern suggesting that some of the yttrium remains unreactive and at high temperatures it reacts with phosphate ion which can block the passage of Li ions[4]. In this case the dopant cannot fully enter the host structure due to the size difference between both dopant and the host cations, this difference develops a strain energy which drives the cation out of the lattice. These cations form oxide phases and are segregated to the grain boundaries blocking the pathways of lithium ions. However, this material suffers from porosity as it was synthesized by solid state methodology. The pores and cracks in the structure can guide smooth passage for Li ions. Table 5.2 represents the lattice parameters of LATP, LAYTP and LAYTSP sample sintered at 900 °C, the lattice parameters increase as Y^{+3} and Si^{+4} are doped in LATP structure.

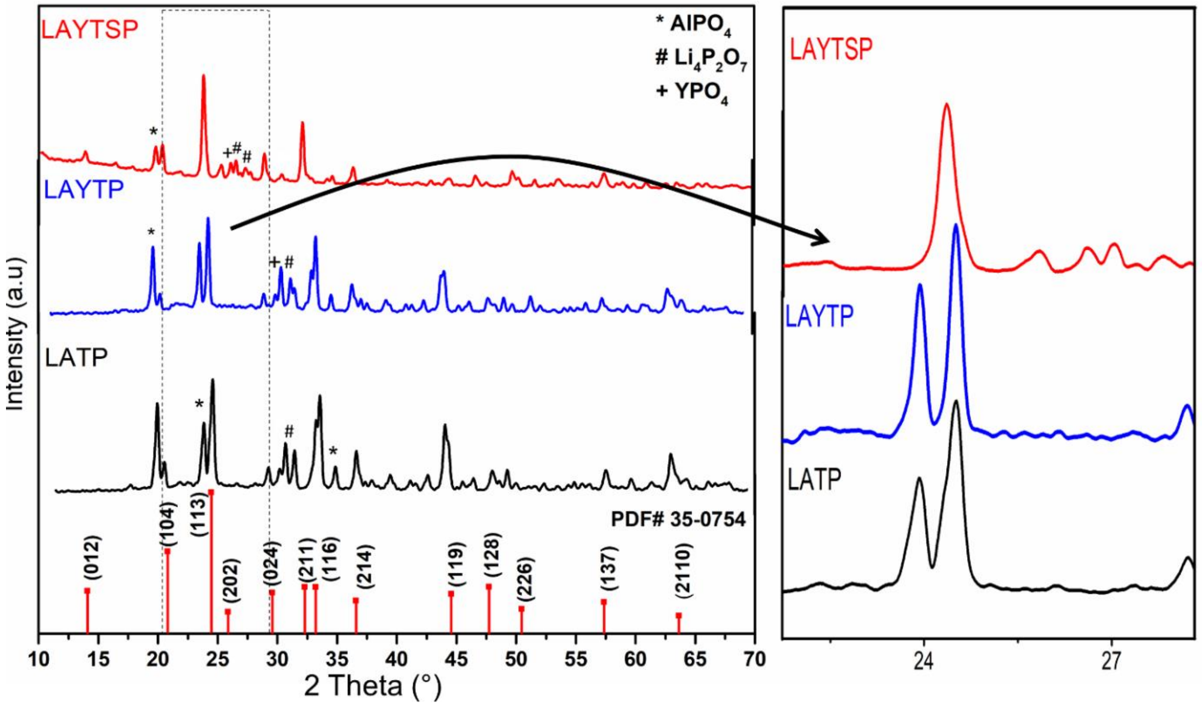

Figure 5.2: XRD pattern of LATP, LAYTP and LAYTSP at 900 °C.

Table 5.2: Lattice parameters of LATP, LAYTP AND LAYTSP.

SAMPLE	lattice parameters(Å)			Volume
	a	b	c	$Å^3$
LATP	8.49	8.49	20.8403	1303.50
LAYTP	8.50	8.50	20.8464	1304.63
LAYTSP	8.409	8.409	21.807	1335.569

5.1.2 Morphological analysis

SEM micrographs and EDX spectra of as-prepared LAYTSP powders synthesized at 900 °C, LATP and LAYTP are shown in Figure 5.3(A, D and G). The LATP and LAYTP show a mixed morphology with small crystals which can be due to low crystallinity of the as-prepared sample. However, the SEM image of LAYTSP shows hexagonal particles as can be seen in Figure 5.3(A). The average particle size of LAYTSP is 1.43 µm deduced from the histogram in Figure 5.3(B). The presence of secondary phase $AlPO_4$ forms microcracks within the LATP structure. These cracks do not affect the microstructure of LATP and neither effect the ionic conductivity [53]. The LAYTSP has a homogeneous and dense mesoporous structure, indicating that the samples may have a high density, which could lead to improved performance. The small crystals on the surface represent impurity phases. With increasing temperature these impurity phases increase and block the lithium conducting passages resulting in grain boundary conductivities[37]. These phases exist less in the LAYTSP structure. In LAYTSP, large particles form a compact structure that allows it to avoid the undesirable effects of the impurity phase $AlPO_4$ on the boundary conductivity [49]. The presence of $AlPO_4$ phase, large particle sizes and dense structure can increase the migration of Li^+ ions by reducing the resistance at grain bounary.

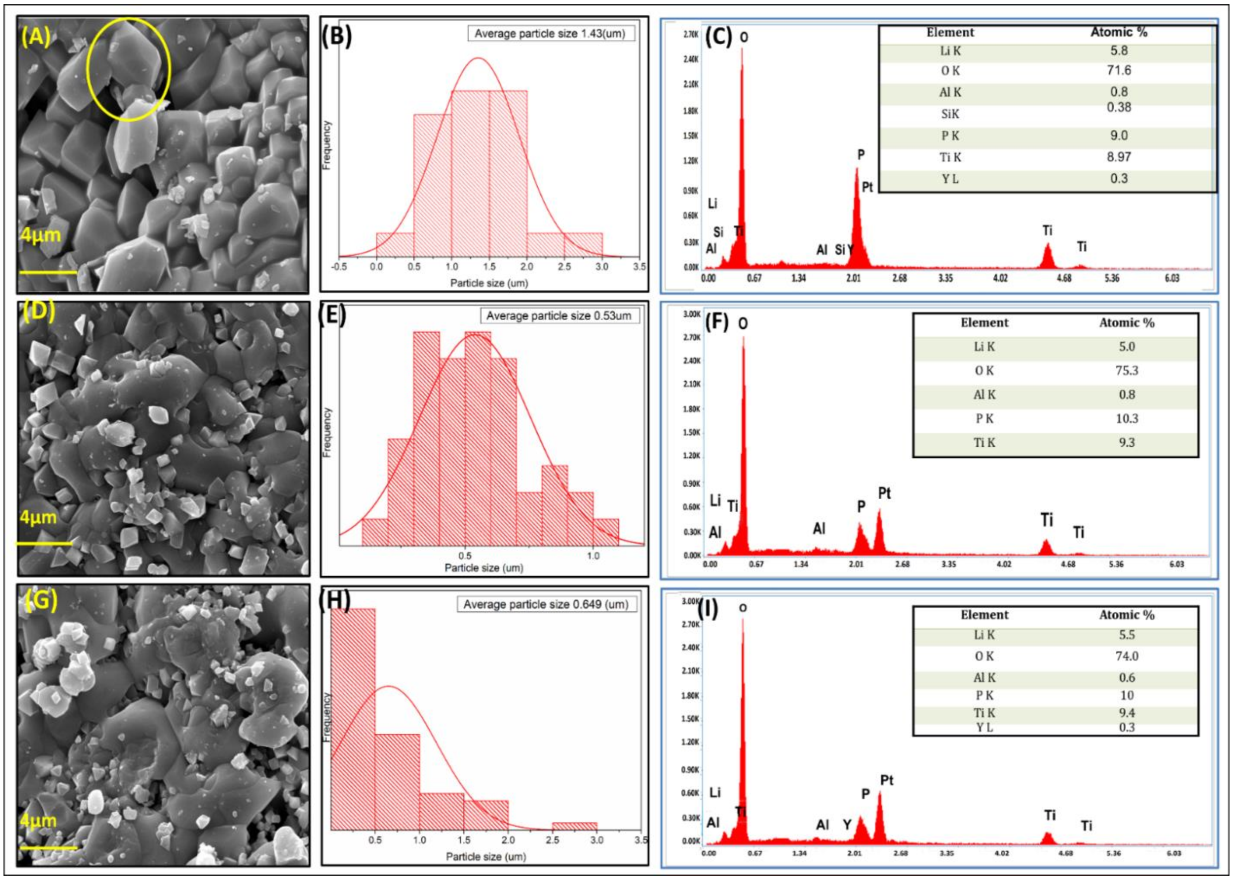

Element	Atomic %
Li K	5.8
O K	71.6
Al K	0.8
SiK	0.38
P K	9.0
Ti K	8.97
Y L	0.3

Element	Atomic %
Li K	5.0
O K	75.3
Al K	0.8
P K	10.3
Ti K	9.3

Element	Atomic %
Li K	5.5
O K	74.0
Al K	0.6
P K	10
Ti K	9.4
Y L	0.3

Figure 5.3: SEM images at 4 µm resolution of (A)LAYTSP, (D) LATP, (G) LAYTP.

Furthermore, the EDX spectra of LAYTSP powder shows the presence of elements of which it is comprised of i.e., O, Ti, P, Al, Li, Y, and Si with weight percentage corresponding to the ionic concentrations that point towards the successful preparation of the as-synthesized sample. The normal distribution curve of particle sizes for each sample are plotted in sub-images (B). The particle size in LAYTSP distribution curve lies between 1.3-1.7 µm. Similarly, the particle size in case of LATP and LAYTP lies between 0.4-0.8 µm and 0.4-1.0 µm respectively. The distribution curve in case of LATP Figure 5.3 (E) shows the average particle size 0.53 µm and the average particle size in LAYTP is 0.649 µm Figure 5.3 (H). It is observed and is in correspondence with the xrd results that the doping of Y and Si increases the particle size of LATP structure.

5.1.3 Absorption analysis

Figure 5.4 shows the FTIR spectra of LAYTSP in range from 4500 to 500 cm^{-1} wavenumbers. The band at 1225 cm^{-1} corresponds to PO_4 ionic vibrations and the band at 1042 cm^{-1}

corresponds to the stretching of $(PO_4)^{-3}$ ions, also the band at 825cm^{-1} corresponds to the vibrations of O-P-O bond [9]. The bands at 1142 cm^{-1} and 990.87 cm^{-1} are attributed to the vibration of Al-O bond. Similarly, the peak at 802.54 cm^{-1} corresponds to the symmetric stretching of SiO_2 bond [10]. This could be attributed to the successful doping of silicon in the structure. The bond of yttrium is not visible in this wavenumber range. The band at 1225 cm^{-1} and 1042 cm^{-1} have low peak intensity, this may be due to the doping of Al^{+3}, Y^{+3} and Si^{+4} in the structure or form the effects of sintering. In the FTIR spectrum of LATP and LAYTP, it is observed that the most intense peak is around 1124 cm^{-1}, this band, and the band around 990 cm^{-1} are attributed to the vibration of Al-O bond, the band at 1042 cm^{-1} corresponds to the stretching of $(PO_4)^{-3}$ bonds [11]. In LAYTSP spectrum the intensity of PO_4 band is less, this confirms that the silicon is doped in the structure and affects the P-O bond. No peak of yttrium is detected in this range. Also, no peak of silicon is observed in LATP and LAYTP spectrum.

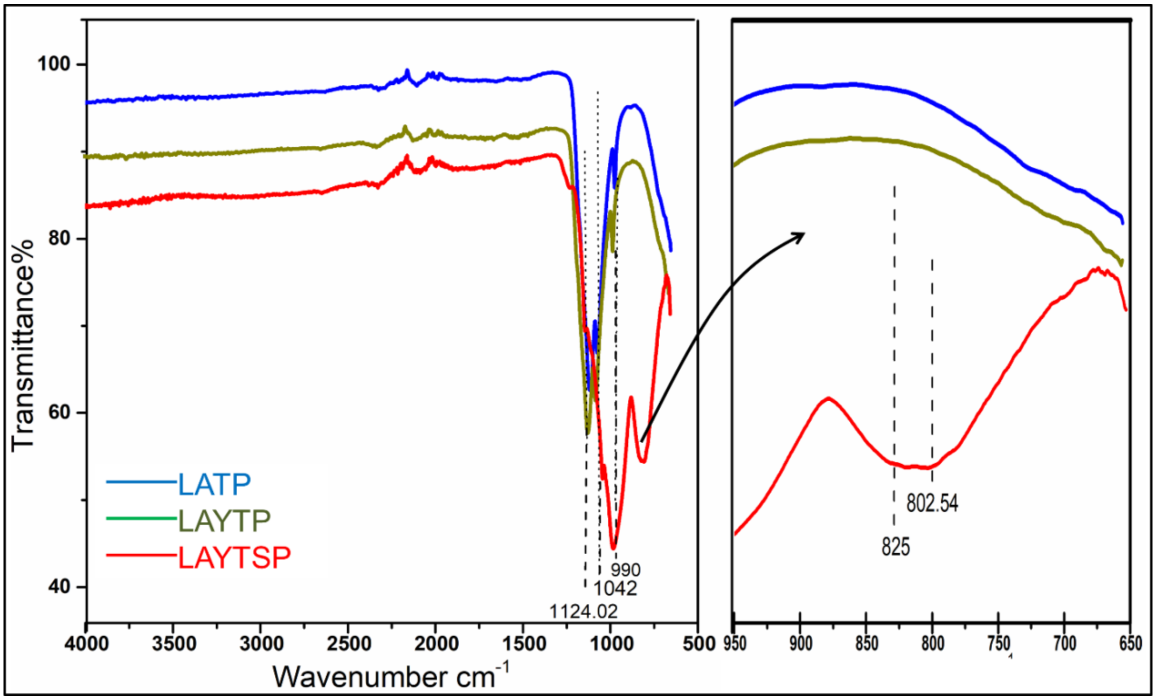

Figure 5.4: FTIR spectrum of LAYTSP, LATP and LAYTP

5.1.4 Compositional analysis

The XPS spectra of samples LATP, LAYTP, and LAYTSP sintered at 900 °C are shown in Figure 5.5. The XPS was performed to evaluate the oxidation state and chemical composition of elements in the respective samples. The atomic concentration of the samples derived from XPS is represented in Table 5.3. The survey spectrum of LATP sample in Figure 5.5(a) shows presence of Li 1s, Al 2p, O 1s, Ti 2p, and P 2p elements. The Al 2p spectrum is shown to deconvolute to only one peak at binding energy (B.E) of 75.2 eV and it corresponds to Al^{+3}. Al exits in single valence state in LATP spectrum [58]. The deconvolution of O 1s shows two peaks at binding energies 531.7 and 528.7 eV which refer to O^{-2} state as in $(PO_4)^{-3}$ and O^{2-} state as in Li_2O. The spectrum of P 2p is deconvoluted in two peaks with B.E of 134.6 eV and 136 eV binding energy. $P2p_{3/2}$ and $P2p_{1/2}$ are the two states in which phosphorous exists in LATP structure[59]. The survey spectrum of LAYTP is shown in Figure 5.5 (b) which confirms the presence of Y in the structure. The deconvolution of Y3d (Figure 5.5 c) shows two peaks around binding energies of 156.3 eV and 157.8 eV which refer to $Y3d_{5/2}$ and $Y3d_{3/2}$ peaks, confirming the existence of Y^{+3} oxidation state [60].

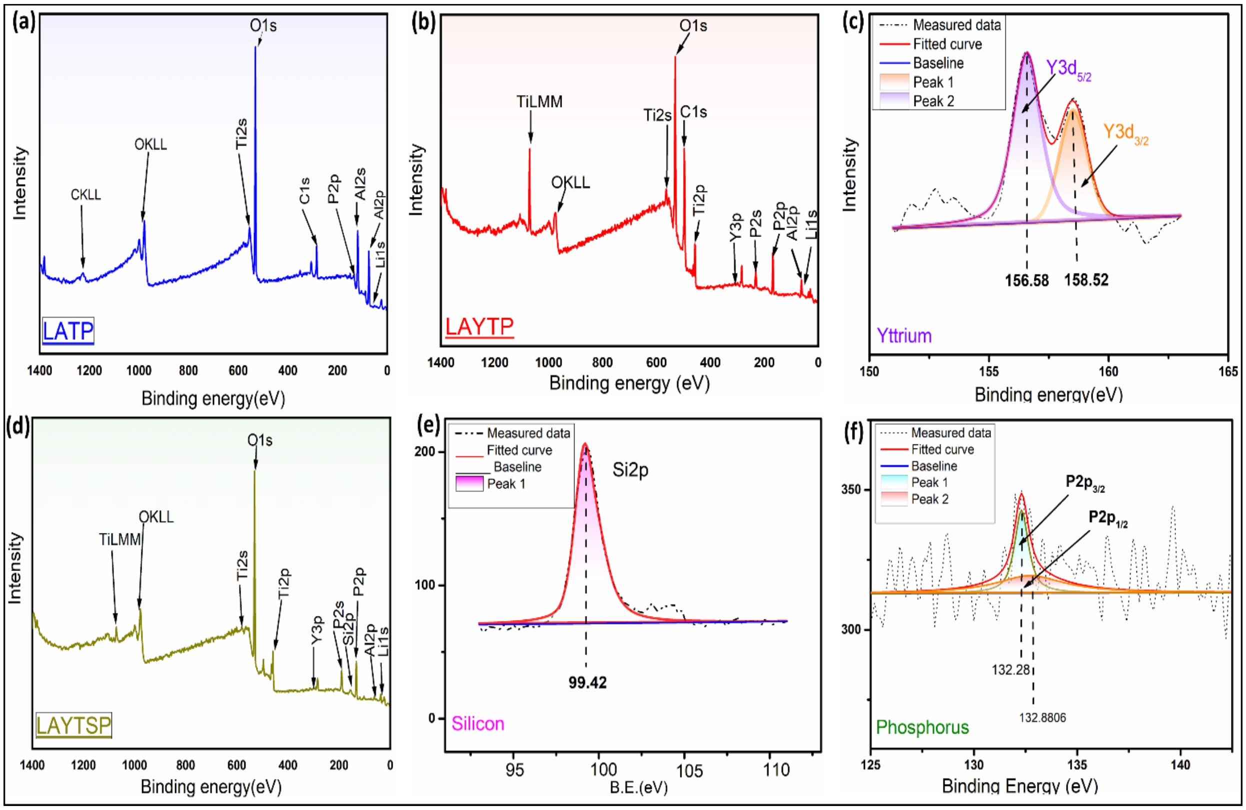

Figure 5.5: XPS spectrum of LATP, LAYTP and LAYTSP sample sintered at 900 °C

Survey spectrum of LAYTSP presented in Figure 5.5(d) shows the presence of Li 1s, Y 3d, Al 2p, Ti 2p, Si 2p, O 1s, and P 2p elements and corroborates well with EDX data. The spectrum of Si 2p shown in Figure 5.5(e) represents a single peak at B.E of 99.4 eV. This peak is attributed to the Si-O bond in which Si exists in +4 oxidation state. The P 2p spectrum in Figure 5.5(f) shows the effect of Si doping at P site, the intensity of P 2p is reduced and the peak is shifted to the binding energies 132.28 eV and 132.88 eV. The $P2p_{1/2}$ peak is reduced and broadens as Si substitutes and disturbs the O-P-O bond of phosphorus[61]. The intensity of lithium increases with concentration and the change in spectrum can be observed from the survey spectra given in in Figure 5.5.

Table 5.3: Atomic concentration of elements in LATP, LAYTP AND LAYTSP lattice.

Sample	**Atomic concentration (%)**						
	Li	Al	Y	Ti	Si	P	O
LATP	1.028	0.256	-	2.177	-	14.75	53.13
LAYTP	3.59	1.34	0.23	9.13	-	15.99	69.73
LAYTSP	8.94	1.22	0.58	8.25	1.43	14.02	62.29

5.2 Electrochemical Performance

The impedance spectra of LATP, LAYTP and LAYTSP samples with different temperature range are depicted in Figure 5.6 (a-e). The impedance spectra show a semicircle at high frequency and an oblique line in the low frequency region. The semicircle originates from the grain boundary properties, and the oblique line demonstrates the diffusion of lithium ions in the blocking Au electrodes. Similarly, the left intercept at high frequency region represents the grain resistance while the grain boundary resistance is represented by diameter of the semicircle. For ionic conductivities an equivalent circuit used to fit these plots as shown in (f). The R_s refers to the bulk resistance, Z_w refers to Warburg impedance, the parallel R_{ct} and CPE_{dl} represents the charge transfer resistance and constant phase element in the semicircle, and the second parallel RC circuit is used for irregular boundaries, impurity phases, and space charges. In (a-c), it is observed that increase in the sintering temperature results in a considerable shift in the impedance values of the LAYTSP solid electrolytes[62]. The grain resistance decreases with increase in temperature as Li ion migration rate increases. Whereas the gain boundary resistance shows a different trend it first increases as temperature increases from 800 °C to 850 °C, then with further temperature increase the grain boundary resistance starts to decrease. This change shows that as temperature increase the impurity phases increase and blocks the Li ion pathways. This behavior of grain boundary resistance shows that some of the dopants are not fully substituted into the structure[63]. The total ionic conductivity is also seen to show the same behavior as the grain boundary resistance. The total ionic conductivity of LAYTSP pellets is shown in Table 5.4.

In comparison, Figure 5.6 (d and e) represents the LATP and LAYTP Nyquist plots. Table 5.5 shows the values of R_s, R_{ct}, and ionic conductivities of LATP, LAYTP and LAYTSP sintered at 900 °C. The LAYTP plot shows a compressed semicircle due to the roughness of the surface but still it has the highest ionic conductivity values. LATP has the lowest ionic conductivity value as compared to doped solid-electrolyte materials. With the doping of Y in LATP structure the volume of Li conduction pathways increases which reduces the hindrance in the migration of Li ions. The grain boundary resistance is also decreased with Y doping. In LAYTSP the ionic conductivity is less although its grain resistance is very less from LATP and LAYTP, the reason is the grain boundary resistance. With co-doping of both Y and Si in the structure the formed impurity phases segregate towards the grain boundary and block the Li ion pathways. The novel LAYTSP has lowest grain impedance value than the base material LATP and LAYTP synthesized by solid-state method.

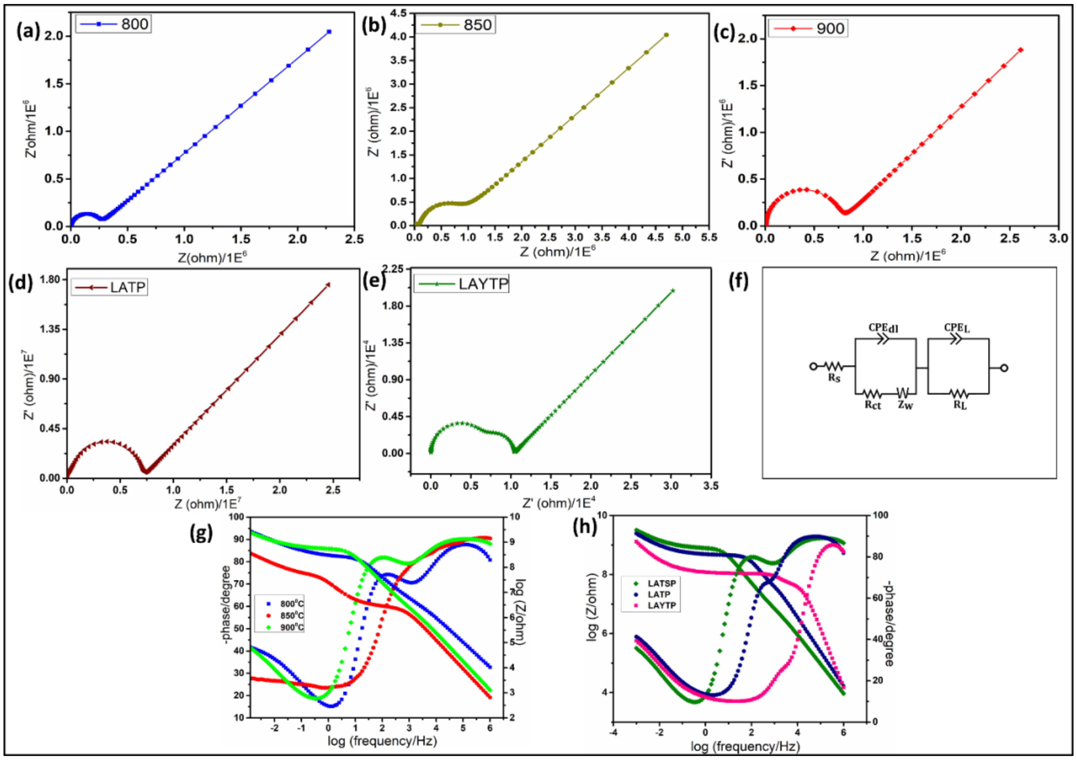

Figure 5.6: Nyquist plots of LAYTSP (a) 800 °C, (b) 850 °C, (c) 900 °C. (d) LATP and (e) LAYTP.

Table 2: Ionic conductivity of LAYTSP samples

Sintering temperature °C	**Rs Ω**	**Rct Ω**	**Ionic conductivity S/cm at RT**
800	1652	1.707×10^{6}	1.57×10^{-5}
850	587.7	6.814×10^{6}	3.94×10^{-6}
900	523.8	2.268×10^{6}	1.18×10^{-5}

Table 3: Ionic conductivities of LATP and LAYTP

Material	**Rs Ω**	**Rct Ω**	**Ionic conductivity S/cm at RT**
LATP	1929	6.52×10^{7}	4.12×10^{-7}
LAYTP	1658	3.689×10^{5}	7.25×10^{-5}
LAYTSP	523.8	2.268×10^{6}	1.18×10^{-5}

The bode plots of LAYTSP samples sintered at different temperatures is shown in Figure 5.6 (g) and the bode plots of LATP, LAYTP in comparison with LAYTSP sintered at 900 °C is given in 5.6 (h). There plots show similar trends of conductivity as expressed in Nyquist plot[18]. Figure 5.8 represents the comparison of grain and toral conductivities of each sample. The grain conductivity shows an increasing trend with increase in sintering temperature of LAYTSP sample with temperature increase more lithium ions are available for conduction. The doping of yttrium ions forms impurity phases like YPO_4 segregates at grain boundaries and tend to bind together the grains increasing the compact density[11]. However, if the impurity concentration increases these phases agglomerates and blocks the conduction pathways of Li ions.

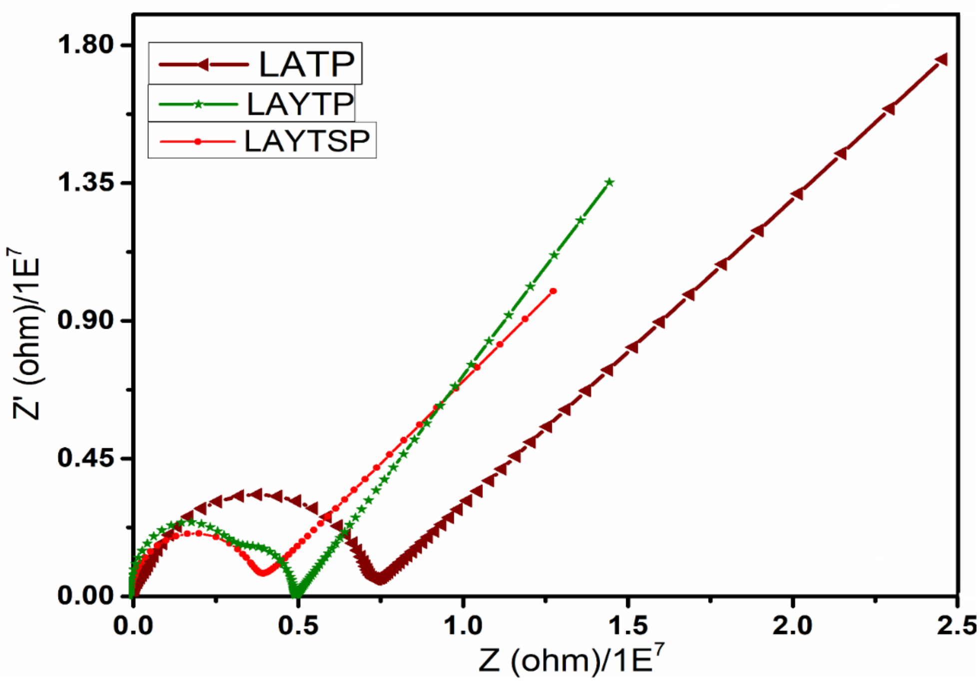

Figure 5.7: Comparison of Nyquist plot of LATP, LAYTP and LAYTSP samples

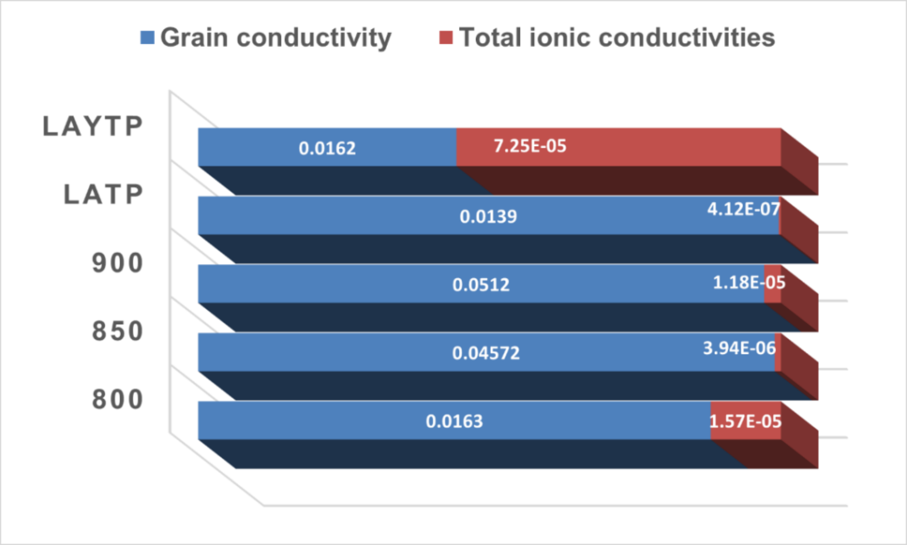

Figure 5.8: The comparison of grain conductivities and total conductivities of LATP, LAYTP and LAYTSP samples at 800 °C, 850°C and 900 °C.

Summary

All the results obtained during the research are discussed in this chapter. Characterization results of XRD, SEM, EDS, FTIR, and XPS are supported with facts from previous studies and justified to understand the morphology, structure, composition, thermal stability, functional groups, surface area and porosity of the synthesized materials. Electrochemical results of the synthesized electrodes are discussed at the end. All the results are presented after comparison with the literature and are supported in the light of properties from characterization techniques.

List of References

[1] T. Hupfer *et al.*, “Evolution of microstructure and its relation to ionic conductivity in Li1+xAlxTi2-x(PO4)3,” *Solid State Ionics*, vol. 288, pp. 235–239, 2016, doi: 10.1016/j.ssi.2016.01.036.

[2] S. Yu *et al.*, “Influence of microstructure and AlPO4 secondary-phase on the ionic conductivity of Li1.3Al0.3Ti1.7 (PO4)3 solid-state electrolyte,” *Funct. Mater. Lett.*, vol. 9, no. 5, pp. 1–6, 2016, doi: 10.1142/S1793604716500661.

[3] Z. Kou, C. Miao, Z. Wang, and W. Xiao, “Novel NASICON-type structural Li1.3Al0.3Ti1.7SixP5(3-0.8x)O12 solid electrolytes with improved ionic conductivity for lithium ion batteries,” *Solid State Ionics*, vol. 343, no. August, p. 115090, 2019, doi: 10.1016/j.ssi.2019.115090.

[4] E. Zhao *et al.*, “High ionic conductivity Y doped Li1.3Al0.3Ti1.7(PO4)3 solid electrolyte,” *J. Alloys Compd.*, vol. 782, pp. 384–391, 2019, doi: 10.1016/j.jallcom.2018.12.183.

[5] D. H. Kothari and D. K. Kanchan, “Effect of doping of trivalent cations Ga3+, Sc3+, Y3+ in Li1.3Al0.3Ti1.7 (PO4)3 (LATP) system on Li+ ion conductivity,” *Phys. B Condens. Matter*, vol. 501, pp. 90–94, 2016, doi: 10.1016/j.physb.2016.08.020.

[6] P. Y. Yen, M. L. Lee, D. H. Gregory, and W. R. Liu, “Optimization of sintering process on Li1+xAlxTi2-x(PO4)3 solid electrolytes for all-solid-state lithium-ion batteries,” *Ceram. Int.*, vol. 46, no. 12, pp. 20529–20536, 2020, doi: 10.1016/j.ceramint.2020.05.162.

[7] M. Liu *et al.*, “Facile synthesis and electrochemical properties of high lithium ionic conductivity Li1.7Al0.3Ti1.7Si0.4P2.6O12 ceramic solid electrolyte,” *J. Alloys Compd.*, vol. 756, pp. 103–110, 2018, doi: 10.1016/j.jallcom.2018.04.333.

[8] X. Liu, J. Fu, and C. Zhang, “Preparation of NASICON-Type Nanosized Solid Electrolyte Li1.4Al0.4Ti1.6(PO4)3 by Evaporation-Induced Self-Assembly for Lithium-Ion Battery,” *Nanoscale Res. Lett.*, vol. 11, no. 1, pp. 0–4, 2016, doi: 10.1186/s11671-016-1768-z.

[9] Y. L. Ruan, K. Wang, S. D. Song, X. Han, and B. W. Cheng, “Graphene modified sodium vanadium fluorophosphate as a high voltage cathode material for sodium ion batteries,” *Electrochim. Acta*, vol. 160, no. December, pp. 330–336, 2015, doi:

10.1016/j.electacta.2015.01.186.

[10] T. N. Tran, T. V. A. Pham, M. L. P. Le, T. P. T. Nguyen, and V. M. Tran, “Synthesis of amorphous silica and sulfonic acid functionalized silica used as reinforced phase for polymer electrolyte membrane,” *Adv. Nat. Sci. Nanosci. Nanotechnol.*, vol. 4, no. 4, 2013, doi: 10.1088/2043-6262/4/4/045007.

[11] M. I. Kimpa *et al.*, “Sol-Gel Synthesis and Electrical Characterization of Li1 + xAlxTi2-x (PO4) 3 Solid Electrolytes Sol-Gel Synthesis and Electrical Characterization of Li 1 + x Al x Ti 2- x (PO 4) 3 Solid Electrolytes,” no. January 2018, 2017.

[12] Z. Kou, C. Miao, Z. Wang, and W. Xiao, “Novel NASICON-type structural Li1.3Al0.3Ti1.7SixP5(3-0.8x)O12 solid electrolytes with improved ionic conductivity for lithium ion batteries,” *Solid State Ionics*, vol. 343, no. September, p. 115090, 2019, doi: 10.1016/j.ssi.2019.115090.

[13] S. Wang, Y. Ding, G. Zhou, G. Yu, and A. Manthiram, “Durability of the Li1+xTi2-xAlx(PO4)3 Solid Electrolyte in Lithium-Sulfur Batteries,” *ACS Energy Lett.*, vol. 1, no. 6, pp. 1080–1085, 2016, doi: 10.1021/acsenergylett.6b00481.

[14] A. Kizilaslan, M. Kirkbinar, T. Cetinkaya, and H. Akbulut, “Sulfur doped Li1.3Al0.3Ti1.7(PO4)3solid electrolytes with enhanced ionic conductivity and a reduced activation energy barrier,” *Phys. Chem. Chem. Phys.*, vol. 22, no. 30, pp. 17221–17228, 2020, doi: 10.1039/d0cp03442h.

[15] G. Yan *et al.*, “Influence of sintering temperature on conductivity and mechanical behavior of the solid electrolyte LATP,” *Ceram. Int.*, vol. 45, no. 12, pp. 14697–14703, 2019, doi: 10.1016/j.ceramint.2019.04.191.

[16] E. Yi, W. Wang, S. Mohanty, J. Kieffer, R. Tamaki, and R. M. Laine, “Materials that can replace liquid electrolytes in Li batteries: Superionic conductivities in Li1.7Al0.3Ti1.7Si 0.4P2.6O12. Processing combustion synthesized nanopowders to free standing thin films,” *J. Power Sources*, vol. 269, pp. 577–588, 2014, doi: 10.1016/j.jpowsour.2014.07.029.

[17] J. Zhu *et al.*, “Insights into the local structure, microstructure and ionic conductivity of silicon doped NASICON-type solid electrolyte Li1.3Al0.3Ti1.7P3O12,” *Energy Storage Mater.*, vol. 44, pp. 190–196, 2022, doi: 10.1016/j.ensm.2021.10.003.

[18] C. R. Mariappan, M. Gellert, C. Yada, F. Rosciano, and B. Roling, "Grain boundary resistance of fast lithium ion conductors: Comparison between a lithium-ion conductive Li-Al-Ti-P-O-type glass ceramic and a Li 1.5Al0.5Ge1.5P3O12 ceramic," *Electrochem. commun.*, vol. 14, no. 1, pp. 25–28, 2012, doi: 10.1016/j.elecom.2011.10.022.

Chapter: 6 Conclusions and Recommendations

6.1 Conclusions

Novel Si^{+4} and Y^{+3} doped $Li_{1.7}Al_{0.225}Y_{0.075}Ti_{1.7}Si_{0.4}P_{2.6}O_{12}$ LAYTSP is successfully synthesized by conventional solid-state method. The base material LATP and single doped LAYTP electrolyte pellets were also synthesized by same method for comparison with novel electrolyte. The new electrolytes have a high crystalline structure and low impurity phases than undoped and only Y^{+3} substituted samples. Hexagonal phase is formed, and the electrolyte has less pores and cracks formation. The ionic conductivity is $1.81e^{-5}$ S/cm at room temperature which is greater than the LATP system. The ionic conductivity can further be improved by using different synthesis techniques such as sol gel, melt quenching and microwave assisted sintering techniques. The LAYTSP can successfully be incorporated as a solid electrolyte in ASSLBs in future.

6.2 Recommendations

The electrochemical performance and efficiency of ASSLBs can be increased by exploring new combinations of materials to be employed as electrolytes, in addition to the informed selection of electrode materials. The following recommendations are presented to address the shortcomings in the research regarding the solid electrolyte materials:

- Focus of the future research should be towards the various tetravalent cations and a hybrid oxide and sulfide-based structure to offer stability and high electrochemical performance for ASSLBs.
- Ceramics and polymer composites should be explored to enhance the stretch, flexibility, and ionic conductivities of the electrolytes.
- In contrast to traditional Li-ion batteries, ASSLBs lack the required power density. Therefore, research is required in the direction of sodium ion batteries to ensure maximum power density and energy density simultaneously.

Appendix: Publications

Investigation of electrochemical properties of Y and Si co-doped $Li_{1.3}Al_{0.3}Ti_{1.7}(PO_4)_3$ solid electrolyte for lithium batteries

Hirra Anwar,[a] Zeeshan Ali,[b] Ghulam Ali,[a,]*

[a]U.S.-Pakistan Center for Advanced Studies in Energy (USPCASE), National University of Sciences and Technology (NUST), H-12, Islamabad, 44000, Pakistan.

[b]School of Chemical and Materials Engineering (SCME), National University of Sciences and Technology (NUST), H-12, Islamabad, 44000, Pakistan.

Abstract

Doping of superfast ionic conductors like NASICON has been shown to improve ionic conductivity and hence the performance of batteries. In this work, NASICON-type yttrium and silicon doped lithium aluminum titanium phosphate (LATP) solid electrolytes are synthesized via the conventional solid-state method at different sintering temperatures. Their intrinsic physical, chemical, and electrochemical properties are investigated using X-ray diffraction, scanning electron microscope, Fourier transform infrared spectroscopy, X-ray photoelectron spectroscopy, and electrochemical impedance spectroscopy. It has been observed that the yttrium and silicon co-doped LATP (LAYTSP) powder sintered at 900 °C exhibits homogeneous hexagonal morphology and outstanding crystallinity than the pristine LATP powder, demonstrating a higher ionic conductivity of 1.81×10^{-5} S cm^{-1} at room temperature. The temperature dependency on the structural morphology and Li^+ ion mobility of LAYTSP has been investigated thoroughly.

Keywords: Lithium-ion batteries; LATP; lithium-ion batteries; solid electrolyte; NASICON

Journal: Journal of Alloys and Compounds

Impact Factor: 5.316

Status: Under Review